

ATG9 resides on a unique population of small vesicles in presynaptic nerve terminals

Beyenech Binotti, Momchil Ninov, Andreia P. Cepeda, Marcelo Ganzella, Ulf Matti, Dietmar Riedel, Henning Urlaub, Sivakumar Sambandan & Reinhard Jahn

To cite this article: Beyenech Binotti, Momchil Ninov, Andreia P. Cepeda, Marcelo Ganzella, Ulf Matti, Dietmar Riedel, Henning Urlaub, Sivakumar Sambandan & Reinhard Jahn (26 Oct 2023): ATG9 resides on a unique population of small vesicles in presynaptic nerve terminals, *Autophagy*, DOI: [10.1080/15548627.2023.2274204](https://doi.org/10.1080/15548627.2023.2274204)

To link to this article: <https://doi.org/10.1080/15548627.2023.2274204>



© 2023 The Author(s). Published by Informa UK Limited, trading as Taylor & Francis Group.



[View supplementary material](#)



Published online: 26 Oct 2023.



[Submit your article to this journal](#)



Article views: 1153



[View related articles](#)



[View Crossmark data](#)

ATG9 resides on a unique population of small vesicles in presynaptic nerve terminals

Beyenech Binotti^{a,b*}, Momchil Ninov^{a,c,d*}, Andreia P. Cepeda^d, Marcelo Ganzella^a, Ulf Matti^e, Dietmar Riedel^f, Henning Urlaub^{c,d,g[§]}, Sivakumar Sambandan^{a,h[§]}, and Reinhard Jahn^{a[§]}

^aLaboratory of Neurobiology, Max Planck Institute for Multidisciplinary Sciences, Göttingen, Germany; ^bDepartment of Biochemistry, Biocenter, University of Würzburg, Würzburg, Germany; ^cBioanalytics, Institute of Clinical Chemistry, University Medical Center Göttingen, Germany; ^dBioanalytical Mass Spectrometry, Max Planck Institute for Multidisciplinary Sciences, Göttingen, Germany; ^eAbberior Instruments GmbH, Göttingen, Germany; ^fFacility for Transmission Electron Microscopy, Max Planck Institute for Multidisciplinary Sciences, Göttingen, Germany; ^gCluster of Excellence "Multiscale Bioimaging: from Molecular Machines to Networks of Excitable Cells" (MBExC), University of Göttingen, Göttingen, Germany; ^hSynaptic Metal Ion Dynamics and Signalin, Max Planck Institute for Multidisciplinary Sciences, Göttingen, Germany

ABSTRACT

In neurons, autophagosome biogenesis occurs mainly in distal axons, followed by maturation during retrograde transport. Autophagosomal growth depends on the supply of membrane lipids which requires small vesicles containing ATG9, a lipid scramblase essential for macroautophagy/autophagy. Here, we show that ATG9-containing vesicles are enriched in synapses and resemble synaptic vesicles in size and density. The proteome of ATG9-containing vesicles immuno-isolated from nerve terminals showed conspicuously low levels of trafficking proteins except of the AP2-complex and some enzymes involved in endosomal phosphatidylinositol metabolism. Super resolution microscopy of nerve terminals and isolated vesicles revealed that ATG9-containing vesicles represent a distinct vesicle population with limited overlap not only with synaptic vesicles but also other membranes of the secretory pathway, uncovering a surprising heterogeneity in their membrane composition. Our results are compatible with the view that ATG9-containing vesicles function as lipid shuttles that scavenge membrane lipids from various intracellular membranes to support autophagosome biogenesis.

Abbreviations: AP: adaptor related protein complex; ATG2: autophagy related 2; ATG9: autophagy related 9; DNA PAINT: DNA-based point accumulation for imaging in nanoscale topography; DyMIN STED: dynamic minimum stimulated emission depletion; EL: endosome and lysosome; ER: endoplasmic reticulum; GA: Golgi apparatus; iBAQ: intensity based absolute quantification; LAMP: lysosomal-associated membrane protein; M6PR: mannose-6-phosphate receptor, cation dependent; Minflux: minimal photon fluxes; Mito: mitochondria; MS: mass spectrometry; PAS: phagophore assembly site; PM: plasma membrane; Px: peroxisome; RAB26: RAB26, member RAS oncogene family; RAB3A: RAB3A, member RAS oncogene family; RAB5A: RAB5A, member RAS oncogene family; SNARE: soluble N-ethylmaleimide-sensitive-factor attachment receptor; SVs: synaptic vesicles; SYP: synaptophysin; TGN: *trans-Golgi* network; TRAPP: transport protein particle; VT11: vesicle transport through interaction with t-SNAREs.

ARTICLE HISTORY

Received 1 February 2023
Revised 5 October 2023
Accepted 17 October 2023

KEYWORDS

ATG9; autophagy; RAB26; synapse; synaptic vesicles; vesicle proteome



Introduction

Synapses are contact sites between neurons specialized for the transfer of information. During signaling, neurotransmitters are released by exocytosis from synaptic vesicles in the presynaptic compartment. After exocytosis, the vesicle membrane is re-captured by endocytosis. Synaptic vesicles are then locally regenerated involving, at least in some cases, endosomal intermediates [1].

The recycling pathway of synaptic vesicles and the underlying molecular mechanisms are well understood [2,3]. In contrast, less is known about the trafficking pathways responsible for formation, homeostasis, and degradation of synaptic membranes and their resident proteins. While synaptic vesicles


recycle locally during neuronal activity, aged and damaged constituents need to turn over to guarantee continuous functioning of the synapse. Thus, synapses are dependent on slow delivery and removal by axonal transport of membrane vesicles that not only include synaptic vesicles but also other synaptic membranes and their constituents [4]. In recent years there is increasing interest in unraveling the pathways involved in synaptic membrane degradation. Indeed, the lifetimes of synaptic membrane proteins are much shorter than those of synapses [5,6] requiring efficient and selective degradation pathways that are only beginning to be understood.

Eukaryotic cells including neurons possess two main conserved pathways for the degradation of membrane

CONTACT Reinhard Jahn  rjahn@mpinat.mpg.de  Laboratory of Neurobiology, MPI for Multidisciplinary Sciences, Am Fassberg, Göttingen 37077, Germany

*These two authors contributed equally to the work.

[§]Co-corresponding authors.

 Supplemental data for this article can be accessed online at <https://doi.org/10.1080/15548627.2023.2274204>

© 2023 The Author(s). Published by Informa UK Limited, trading as Taylor & Francis Group.

This is an Open Access article distributed under the terms of the Creative Commons Attribution-NonCommercial-NoDerivatives License (<http://creativecommons.org/licenses/by-nc-nd/4.0/>), which permits non-commercial re-use, distribution, and reproduction in any medium, provided the original work is properly cited, and is not altered, transformed, or built upon in any way. The terms on which this article has been published allow the posting of the Accepted Manuscript in a repository by the author(s) or with their consent.

components, which are independent of each other and only converge on lysosomal degradation as the final step [7–9]. The first involves collection of lipids and (frequently ubiquitinated) proteins in early endosomes. They then develop into late endosomes by maturation during which membrane components are sorted out and moved into internal vesicles, mediated by the ESCRT-machinery. As a result, multivesicular bodies are generated that then fuse with lysosomes for final degradation [10]. However, multivesicular bodies are only rarely observed in presynaptic nerve terminals (50 times less frequent than in soma and dendrites [11]), and it remains unclear which role this pathway plays in synaptic membrane turnover. The second pathway, autophagy, involves the formation of membrane-enclosed cisternae that expand into cup-shaped intermediates to which cargo is recruited. They then close, forming an autophagosome engulfing both membranes and cytoplasmic material for lysosomal delivery [12]. Even though many details are still unclear such as the mechanisms responsible for cargo selection and for the formation of autophagosomes, it has become apparent that autophagy is an essential mechanism for maintaining homeostasis of distal axons and synapses [13].

A few years ago, we reported that the GTP form of the small GTPase RAB26, which is specifically localized to a subset of synaptic vesicles, directs entire synaptic vesicles toward pre-autophagocytotic compartments [14]. Moreover, we reported that the autophagy protein ATG16L1 is an effector of RAB26, which is recruited only by the GTP form of RAB26 [14,15]. In addition, PLEKHG5 (pleckstrin homology domain containing, family G (with RhoGef domain) member 5) was identified as a guanine exchange factor for RAB26, thus regulating its activity. Deletion of *Plekhg5*, which shifts all RAB26 into the inactive GDP-form, results in the degeneration of axon terminals and impaired autophagy of synaptic vesicles, which can be rescued by constitutively active RAB26 [16].

The question then arises how autophagosomes are generated in synapses and how this process is regulated? Formation of autophagosomes generally proceeds in distinct steps including (1) nucleation and elongation of a cup-shaped membrane cisterna (phagophore assembly site [PAS]), (2) recruitment of cargo, (3) closure of the PAS, forming an autophagosome surrounded by two membranes enclosing the cargo, and (4) fusion with a lysosome for final degradation. Each of these steps is controlled by a set of ATG (autophagy related) proteins [17,18]. ATG16L1 is recruited to the phagophore membrane after its initial nucleation. It is part of a complex containing, in addition, the proteins ATG12 and ATG5, which together represent an E3-like conjugating system mediating the attachment of ATG8-family proteins such as LC3 to phosphatidylethanolamine (PE) in the growing phagophore membrane [19].

It is still debated from which reservoir the lipids needed for the membrane of the growing autophagosome are originating. Apparently, the autophagy protein ATG9 plays a key role in this process. As the only integral membrane protein essential for autophagosome formation, it was recently identified as a lipid scramblase, which together with the associated

ATG2, a lipid transferase, and additional cofactors may constitute a lipid pump mediating membrane lipid transfer between connected membranes, thus loading up the growing autophagosomal membrane with lipids [20–23]. Intriguingly, ATG2 seems to be confined to contact sites between the endoplasmic reticulum (ER) and the PAS, or between the ER and mitochondria [24], while ATG9 is found in small vesicles which only transiently associate with the PAS [25,26]. Apparently, almost all endomembranes can serve as lipid sources for autophagosome biogenesis [27] but it is not clear how this is achieved.

In neurons, ATG9-containing vesicles appear to be derived from the Trans Golgi network, with their formation requiring the adaptor complex AP3 [28]. They are anterogradely transported toward synapses [29] where the autophagosome biogenesis takes place [30]. Recent work reveals that synaptic ATG9-containing vesicles undergo endo- and exocytosis in activity dependent manner [28] but it is unclear to which extent cycling of ATG9-containing vesicles is related to the cycling of synaptic vesicles and to intrasynaptic trafficking pathways and how exactly they contribute to the growths of autophagosomes.

To obtain a better understanding of neuronal/synaptic ATG9-containing vesicles, we performed a thorough and quantitative characterization of their protein composition. Moreover, we analyzed their relationship to other trafficking organelles using super-resolution fluorescence microscopy at single vesicle resolution both *in vitro* and in intact neurons. In contrast to RAB26-containing vesicles that -as expected- are enriched in synaptic vesicle proteins, ATG9-containing vesicles show no significant overlap with synaptic vesicles or any other trafficking organelle except of a slight enrichment of proteins localized to the plasma membrane. Unlike RAB26 vesicles, ATG9-containing vesicles are not enriched in proteins required for budding, docking or fusion such as coat proteins, tethering factors, RAB-GTPases, or SNARE proteins. Single vesicle analysis confirmed that ATG9-containing vesicles show no significant overlap with proteins characteristic for intracellular trafficking organelles. Moreover, although enriched in presynaptic terminals, they are clearly distinct from synaptic vesicles and their recycling intermediates, establishing them as a unique vesicle population separate from known synaptic trafficking pathways.

Results

ATG9-containing vesicles co-purify with synaptic vesicles but represent a biochemically distinct vesicle population

For a first characterization of ATG9-containing vesicles, we determined the enrichment of ATG9 in different fractions obtained during the isolation of synaptic vesicles from rat brain homogenate [31,32]. In this protocol, isolated nerve terminals (synaptosomes) are first enriched by low-speed centrifugation (P2-fraction, **Figure 1A**), followed by osmotic lysis to release vesicles from the nerve terminals. Membranes are then fractionated by a two-step centrifugation, yielding a lysate pellet 1 (LP1) containing large particles such as resealed synaptosomes, plasma membrane or mitochondria

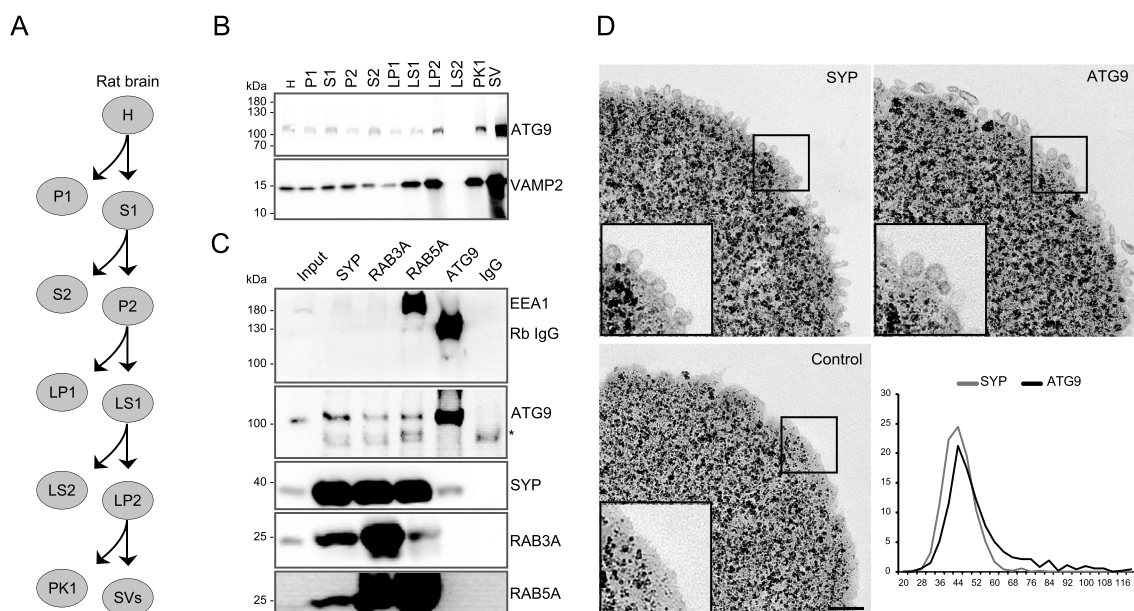


Figure 1. Synaptic ATG9 resides on vesicles resembling synaptic vesicles in size and density but represent a distinct vesicle class. (A) scheme depicting the fractions generated during subcellular fractionation of rat brain during isolation of synaptic vesicles. H, homogenate, P1, P2, and S1, S2, pellets and supernatants, respectively, of the initial centrifugation steps; LP1, LP2, LS1, LS2, pellets and supernatants generated after differential centrifugation of osmotically lysed P2 (synaptosomes); PK1, SV fractions eluted from the final size-exclusion column containing membrane fragments and synaptic vesicles, respectively (see text for details). The supernatant obtained after lysis of synaptosomes (LS1) was used as starting material (input) for the immuno-isolations. (B) immunoblots of fractions (equal amounts of protein loaded) for the vesicle marker VAMP2/SYB2 and ATG9, showing co-enrichment of both proteins during SV isolation. The blot is representative of three biological replicates. (C) immuno-isolation of vesicles using magnetic beads coated with monoclonal mouse antibodies specific for SYP (synaptophysin), RAB3A, RAB5A, and monoclonal rabbit ATG9. Beads coated with sheep IgG were used to control for nonspecific adsorption. Rb IgG band represents the IgGs that were used for immuno-isolation and that cross-react with the detection antibody. Note the cross-reaction of the ATG9 detection antibody with a nonspecific band (asterisk). The blot is representative for at least two biological replicates (see Figure S1). (D) transmission electron microscopy of the magnetic beads after immuno-isolation reveals that ATG9-containing vesicles are very similar (albeit slightly more heterogeneous) to synaptic vesicles. Scale bar: 200 nm. Graph: histogram showing the diameter distribution of ATG9 and SYP vesicles, respectively, bound to the beads. Bar: 200 nm.

fragments and a second pellet (LP2) obtained after ultracentrifugation, which contains small vesicles and other particles, and a membrane-free supernatant (LS2). Synaptic vesicles are then further enriched by consecutive sucrose-density gradient centrifugation and size-exclusion chromatography during which larger fragments elute in the void volume (PK1), followed by a peak containing uniformly sized small synaptic vesicles (SV, for details see [32,33]). Surprisingly, ATG9 copurified with synaptic vesicles (detected using VAMP2/synaptobrevin 2 antibody) suggesting that either ATG9 resides on synaptic vesicles or represents a separate vesicle population with similar size and density at the synapse.

To differentiate between these possibilities, we employed magnetic beads coupled with monoclonal antibodies to selectively isolate the respective membranes from LS1 fractions (Figure 1C, S1). In addition to the starting material, we compared ATG9-immuno-isolates with SV-immuno-isolates using antibodies specific for SYP (synaptophysin; a ubiquitous SV marker), RAB3A (a synaptic vesicle RAB GTPase involved in exocytosis and RAB5A (a RAB-GTPase specific for early endosomes [34,35] that is also involved in synaptic vesicle recycling. Immunoblot analysis of bead-bound vesicles revealed that ATG9 is enriched only in the ATG9 isolates. It is also detectable in the other fractions but at much lower levels. Conversely, SYP, as well as RAB3 and RAB5A, are largely absent from ATG9-immunoisolates. This suggests that despite copurification with synaptic vesicles during subcellular fractionation, the majority of the ATG9-

containing vesicles are distinct from synaptic vesicles and synaptic early endosomes. Analysis of the immuno-isolated vesicles using electron microscopy revealed that the overall size distribution is similar in the two fractions. While the ATG9-containing vesicles contained some larger and elongated vesicles that were absent from the SYP immuno-isolates, the ATG9-containing vesicles are surprisingly homogeneous and similar in size to canonical synaptic vesicles (Figure 1D, graph).

To shed more light on the nature of ATG9-containing vesicles, we determined the proteome of the immuno-isolated ATG9-containing vesicles using label-free quantification mass spectrometry according to standard procedures (see Materials and Methods) and compared it to the proteome of vesicles immuno-isolated with antibodies specific for RAB26.

Analysis of input, ATG9-, RAB26- and IgG control-immuno-isolates together led to the identification of a total of 2859 and 4282 proteins groups in ATG9 and RAB26 datasets, respectively (Table S1 and S2). We then determined the relative enrichments of all quantified proteins recovered in the immuno-isolates with respect to (i) control beads that were coupled to sheep whole IgG, and (ii) the fractions obtained from synaptosomal lysates that were used as starting material (input). The relative enrichments of all quantified proteins are displayed in two-dimensional scatter plots (Figure 2). These plots provide a better overview of the abundance of the proteins co-enriched with ATG9 and RAB26-containing vesicles than the

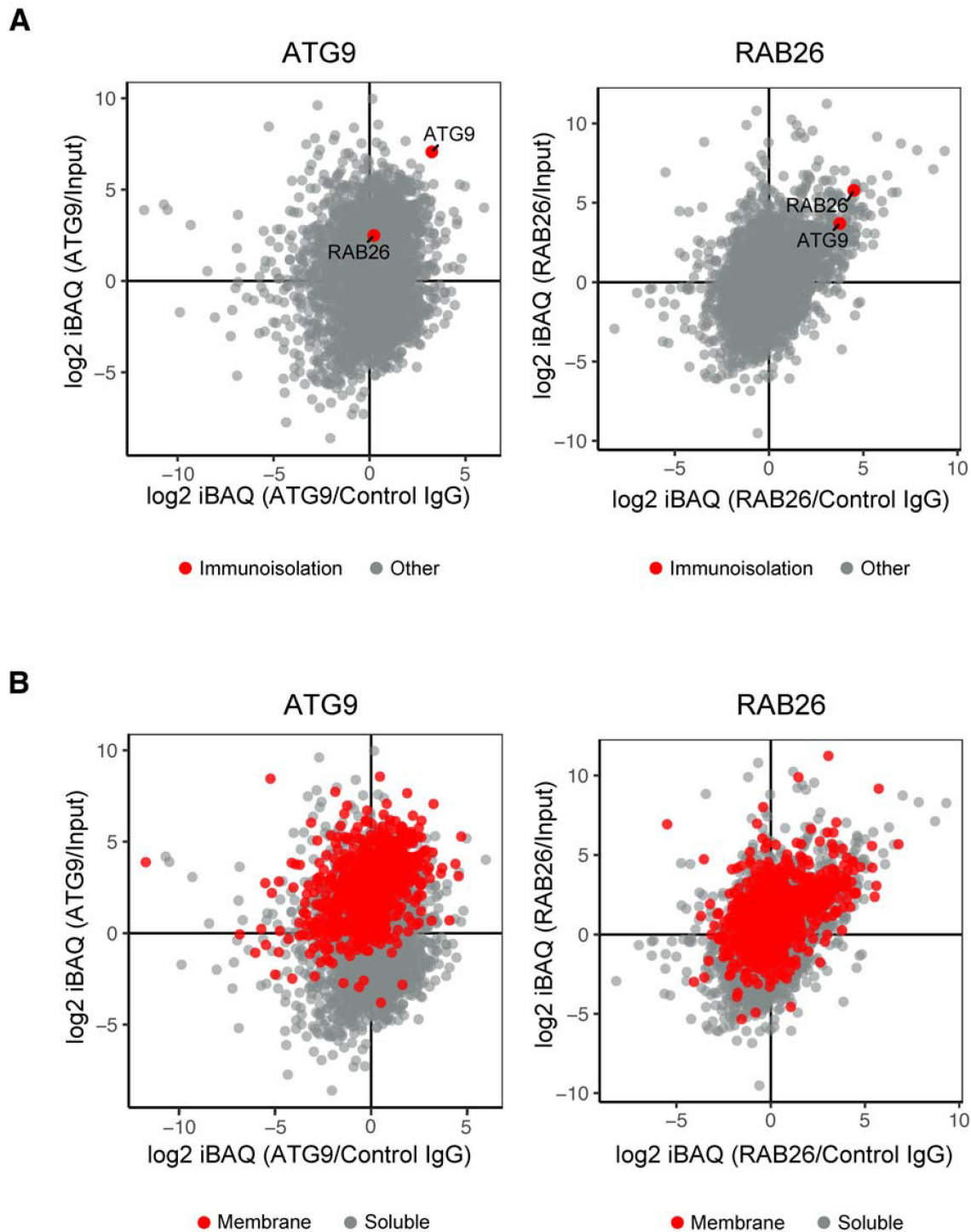


Figure 2. 2D scatter plots of proteins quantified by proteomic analysis of ATG9- and RAB26 immuno-isolates, confirming the purity of the isolated vesicle fractions. (A) overview of all proteins quantified by label-free liquid chromatography-tandem mass spectrometry (LC-MS/MS). The scatter plots represent a 2D comparison of all identified proteins and their log₂-transformed iBAQ values derived from ATG9 (left) and RAB26 (right) immuno-isolates in relation to both reference samples: log₂-transformed iBAQ values of the proteins from starting material for immuno-isolation (Y-axis) and log₂-transformed iBAQ values from proteins on beads coupled to control (sheep) IgG (X-axis). Targeted proteins (ATG9, RAB26, respectively) are highlighted in red. (B) distribution of protein containing transmembrane domains (red dots) in each sample set as plotted under (A).

commonly used volcano plots, with only those proteins that are found in the upper right quadrant being enriched with respect to both reference samples. The high enrichment of ATG9 and RAB26 in the respective bead samples confirm the specificity of our immuno-isolation procedure for the corresponding vesicle populations (Figure 2A).

First, we annotated all integral membrane proteins (Figure 2B and Supplemental table S1 and S2). As expected for immuno-isolation of membrane vesicles, integral membrane proteins are enriched in both data sets. Intriguingly, the enrichment is more conspicuous for ATG9 than for RAB26 isolates. This may be explained by the fact that for ATG9-

containing vesicles LS1 was used as starting material, i.e. a fraction that still contains all proteins of the synaptic cytoplasm whereas RAB26 vesicles were isolated using thoroughly resuspended LP2 as starting material (to avoid antibody saturation by the soluble RAB26 pool), which is enriched in membranes as cytosolic proteins are removed.

To better understand the cellular origin of ATG9-containing vesicles, we determined the enrichment of proteins specific for intracellular organelles. To this end, we manually annotated proteins using recently published high confidence and high-quality curated datasets for individual organelles. These include, in order of categorization: synaptic vesicles (SV) [36], mitochondria (Mito) [37], Lysosomes and endosomes (EL), peroxisomes (Px) [38], plasma membrane (PM), endoplasmic reticulum (ER) and Golgi (GA) [39,40]. The enrichment of these organellar protein markers is displayed in Figure 3A as box plots of the average enrichment (see Figure S2 for the corresponding 2D-plots).

With this type of analysis, several conspicuous patterns are emerging. In agreement with our previous report [14] synaptic vesicle proteins were clearly enriched in the RAB26 immuno-isolates, followed by endosomal/lysosomal markers, and, although barely significant, markers for the plasma membrane (Figure 3A, right). These enrichments confirm that these vesicles represent a subset of synaptic vesicles that is involved in trafficking with the plasma membrane (exocytosis, see [14], and the endo-lysosomal system [41]. In contrast, the profile of ATG9-containing vesicles was more heterogeneous (Figure 3A, left). The highest enrichment was found for proteins localized to the plasma membrane (PM) and, oddly, peroxisomes, whereas all other markers showed only moderate enrichment except of mitochondria that were clearly underrepresented. The lower diagram shows how many of the proteins listed in the curated organelle-specific datasets were recovered (Figure 3A, lower panel). Unsurprisingly, recovery of SV proteins is high in both samples (note that the starting material was already enriched in SVs) whereas only a small subset of mitochondrial or Golgi-associated proteins was recovered (Figure 3A, bottom panels). As additional check for the validity of the quantification method, the enrichment of several top hits on ATG9-containing vesicles was confirmed by immunoblotting (Figure 3B).

As a further test for the validity of the enrichment patterns, we gradually increased the stringency of our analysis by stepwise increasing the enrichment threshold. Most organellar markers showed a linear decline in relative protein number with increasing stringency (Figure S3A and B) resulting in an increased representation of enriched organellar marker proteins in higher cutoffs (Figure S3C). We therefore decided to continue with a high stringency cutoff of 1, corresponding to a 2-fold enrichment, for all further analysis. This cut our list down to 330 proteins for ATG9 (red dots, Figure 3C upper graph), and 513 proteins for RAB26 (purple dots, Figure 3C lower graph) with an overlap of 62 common proteins (Figure 3D). We then asked if the ATG9- and RAB26-vesicle proteomes share proteins specific for common cellular compartments (Figure 3E). The analysis confirms the SV-endosomal signature of the RAB26 vesicles that is not shared

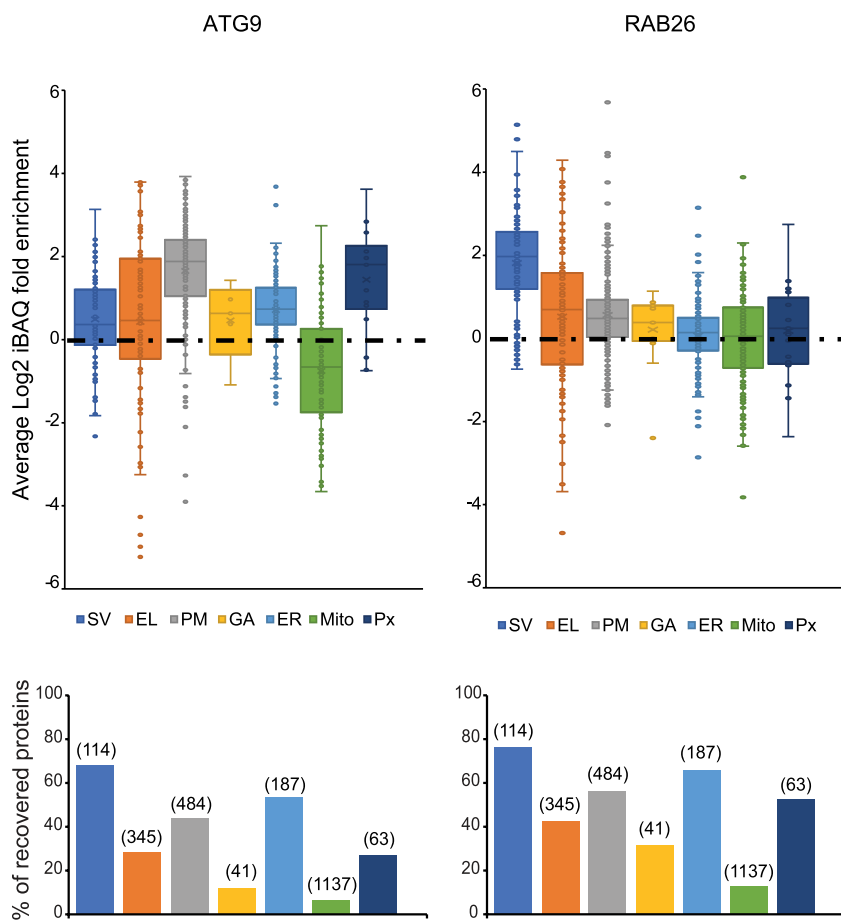
by the ATG9-containing vesicles. In contrast, both ATG9 and RAB26 vesicles contain quite a few plasma membrane proteins (more conspicuous for ATG9-containing vesicles) but show almost no overlap among them (Figure 3E). All these results indicate that ATG9-containing vesicles represent a distinct vesicle population not related to intracellular organelles (with the possible exception of the presynaptic plasma membrane), suggesting that they do not intersect with the SV recycling pathway in the synapse.

ATG9-containing vesicles are largely devoid of proteins involved in budding, targeting, docking and fusion of trafficking vesicles

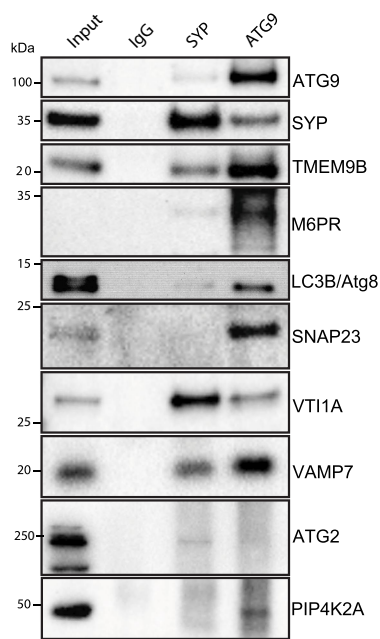
To shed further light on the relationship of ATG9-containing vesicles to intracellular trafficking pathways, we compared the distribution of canonical trafficking proteins involved in vesicle budding, target recognition, docking/tethering, membrane fusion and fission between ATG9 and RAB26 vesicles. (Figure 4). With respect to RAB and SNARE proteins, analysis of the data under high stringency cut-off >1 (Figure 4A,B gray box) revealed major differences between the two vesicle populations. Only four RAB proteins were enriched in the ATG9-containing vesicle proteome: RAB9A and B, which are involved in the recycling of the mannose-6-phosphate receptor, cation dependent (M6PR) between late endosomes and the trans-Golgi network [42,43], and RAB15 and RAB23, which operate in trafficking pathways at the PM [35,44] (Figure 4A upper graph, gray box). In contrast, RAB26 immuno-isolates were enriched for a large set of RABs, similar to synaptic vesicles as previously shown [32,45], with the highest enrichment for the targeted RAB26 itself (Figure 4A lower graph). Similarly, only 3 SNAREs were enriched in ATG9-containing vesicles, each involved in a different trafficking step: SNAP23 functioning at the plasma membrane, the early endosomal SNARE VTI1A, and the late endosomal/lysosomal SNARE VAMP7. In contrast, many SNARE proteins were enriched in RAB26 vesicles, predominantly those functioning in endosome fusion and exocytosis (Figure 4B lower graph, gray box).

To probe deeper into the “trafficking signatures” of the ATG9 and RAB26 vesicles, we compared the enrichment of coat and tethering proteins. For easier comparison, we calculated for the other proteins the average of the enrichment factors in the two dimensions and then displayed their enrichments in heatmap graphs (Figure 4C–H). Both ATG9 and RAB26 appear to be enriched in some of the proteins required for clathrin-mediated endocytosis such as EPN1/Eps1, EPS15 and EPS15L1 and intersectin1/2, as well as the components of the adaptor complex AP2 [46,47] (Figure 4C). On the other hand, we observed no enrichment of other adaptor proteins such as AP1 and AP3, coat proteins such COPI and COPII [48,49] and the retromer complexes [50] (Figure 4C). These results agree with recent observations showing that ATG9-containing vesicles are able to recycle from the presynaptic plasma membrane in a manner similar to SVs, i.e., dependent on synaptic activity [28]. On the other hand, there is a conspicuous absence of tethering factor complexes [51] in the ATG9-containing

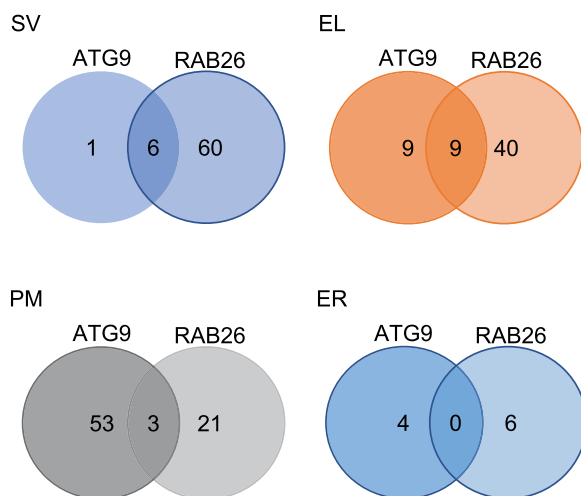
A



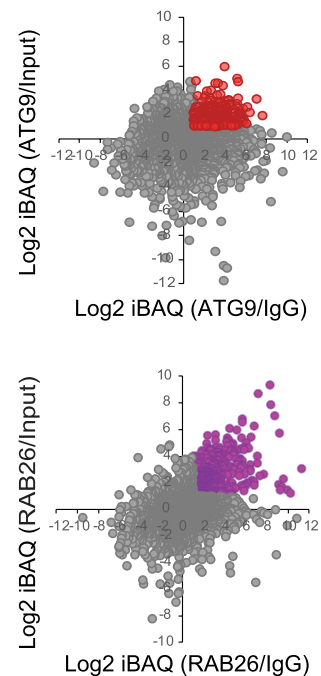
B



E



C



D

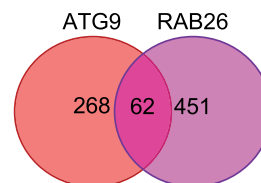


Figure 3. Enrichment of organellar markers in ATG9 and RAB26 vesicles. (A) box plots showing the enrichments of organelle-specific proteins detected in the ATG9 and RAB26 proteome (see Figure S1 for the respective 2D scatter plots). SV, synaptic vesicles (blue), EL, endosomes and lysosomes (orange), PM, plasma membranes (gray), GA, Golgi apparatus (yellow), ER, endoplasmic reticulum (light blue), Mito, mitochondria (green), Px, peroxisomes (dark blue). The Y-axis shows the average log₂-fold enrichment (log₂ iBAQ ATG9/Input + log₂ iBAQ ATG9/control IgG) divided by 2 of the individual proteins of each group. Bottom: graphs representing the fraction (in %) of the proteins listed in the respective organelle database (see text for details) that were recovered in the respective immuno-isolates (the numbers on

vesicle proteome (Figure 4D). This is in stark contrast to the proteome of the RAB26 immuno-isolates which show enrichment of several tethering complexes including the HOPS complex (late endosome – lysosome/autophagosome [52], TRAPPI (ER – Golgi), TRAPPII (Golgi – PM) and TRAPPIII (ER – PAS) [53,54].

Furthermore, for the RAB26 vesicles an endolysosomal signature was supported by the enrichment of ESCRTIII subunits [10] (Figure 4E), and the Ragulator-MTORC1 supercomplex [55] (Figure 4F). ATG9-containing vesicles instead show only a mild enrichment of a subset of ESCRT III subunits and the Ragulator complex (without MTORC1 components) confirming again that ATG9-containing vesicles do not display a strong lysosomal signature. Note that also the V-ATPase [56] appears to be lacking from ATG9-containing vesicles (Figure 4G) suggesting that their lumen does not acidify, again different from all post-Golgi trafficking vesicles.

Finally, we analyzed the enrichment of autophagy proteins in both immuno-isolates. Interestingly, while RAB26 vesicles were enriched in factors involved in the early steps of autophagosome formation (ATG2, ULK1, PIK3C3) ATG9-containing vesicles instead contained LC3 isoforms and the autophagy receptor p62 (Figure 4H). This suggests that RAB26 vesicles are involved at the early steps of autophagy as described previously [14,15], while ATG9-containing vesicles act in later stages of autophagosome formation.

Single vesicle imaging by superresolution microscopy reveals heterogeneity of ATG9-containing vesicles, showing only limited overlap with synaptic and other trafficking vesicles

The data presented so far show that in synapses ATG9 resides on a population of vesicles similar in size and density to SVs but quantitatively different in their protein composition, with no or only moderate enrichment of membrane proteins specific for distinct intracellular membranes. However, with such bulk approaches it is not possible to discern whether ATG9-containing vesicles are biochemically homogeneous (as previously shown for SVs) or heterogeneous, i.e., consisting of subpopulations distinguished by their protein composition. To address this issue, we performed single vesicle imaging of rat brain vesicle preparations using Dynamic minimum stimulated emission depletion (DyMIN STED) microscopy [57]. DyMIN STED is a newly developed adaptive optics STED technique that provides super-resolution with reduced photobleaching and enhanced fluorescence detection from single vesicles [58]. We also combined the

imaging with a novel labeling strategy to maximize the epitope coverage and to remove background fluorescence. Freshly isolated vesicles were labeled using saturating concentrations of the antibody “in-solution,” followed by an additional size exclusion chromatography (SEC) step to remove unbound antibodies (Figure 5A). Thus, the combination of DyMIN STED and the efficient labeling procedure allowed high-throughput and quantitative analysis of single vesicles.

First, we performed three-color DyMIN STED imaging of vesicles following immunolabeling for ATG9, SYP and VAMP2/synaptobrevin 2 (vesicle-associated membrane protein 2) markers that are present in all SVs (Figure 5B). A coordinate-based colocalization analysis [57] revealed that SYP and VAMP2 vesicles, as expected, exhibited a complete overlap. However, ATG9 was only occasionally colocalized with the SV markers with only ~2% SYP and VAMP2 vesicles carrying ATG9 (Figure 5B). Next, we examined colocalization of ATG9, SYP, and one of the following proteins (except of RAB26, all integral membrane proteins): the SNARE VTI1B, LAMP2 and the aminophospholipid flippase ATP8A1 for endo/lysosomes, the P/Q type voltage-dependent calcium channel CACNA1A for presynaptic plasma membrane, M6PR for trafficking vesicles between the Golgi and endosomes, the protein translocon subunit SEC61A1 for endoplasmic reticulum, LAMP5 for non-canonical synaptic endosomes, and RAB26. As expected, the vesicle preparation was markedly enriched for synaptic vesicles (as detected by SYP), but distinct pools of ATG9, organellar and other trafficking membrane signatures were conspicuously detected (Figure C). We found that none of the organellar markers showed major overlap with either ATG9 or SYP, except for RAB26 which exhibited strong overlap with SYP (Figure 5C), again confirming the previous observations.

Several conclusions can be drawn from these data. Most importantly, they document that synaptic ATG9-containing vesicles, despite their morphological homogeneity, are highly heterogeneous in their membrane composition, with all tested proteins, including SYP and RAB26, being clearly detectable, but only on minor subpopulations of ATG9-containing vesicles (between 0.2% and 10.3% of all ATG9-containing vesicles). Moreover, triple labeling allowed for the distinction of 7 different subpopulations in each case (Figure 5), revealing that all analyzed proteins can be found on subpopulations containing either ATG9, SYP, both proteins, or none of them, thus showing a high degree of heterogeneity. Intriguingly, for SYP vesicles (that dominate the sample) the degree of overlap with any of the other proteins (except of RAB26) is considerably lower than for ATG9-containing vesicles. Overall, the above

top of the bars represent the total number of proteins in the organelle proteomes). (B) distribution of selected proteins between vesicles immuno-isolated for SYP and ATG9, respectively. Immuno-isolated fractions were analyzed by immunoblotting for select proteins, confirming MS-based quantification of proteins enriched in ATG9-containing vesicles. These include TMEM9B, M6PR, LC3B, SNAP23, VTI1A, VAMP7, ATG2A and PIP4K2A found in ATG9-containing vesicles compared to Synpatophysin vesicles. See Figure 1 for details. (C) scatter plot showing the proteins enriched > 2-fold in both dimensions, corresponding to a cutoff of log₂-transformed iBAQ (ATG9/Control) and (ATG9/Input) > 1, for both ATG9 (red, upper graph) and RAB26 (violet, lower graph). (D) Venn diagram of the > 2-fold enriched proteins in the ATG9 (red) and RAB26 (violet) proteome showing that overlap is limited. (E) as in (C) but limited to the recovered organelle-specific proteins, respectively.

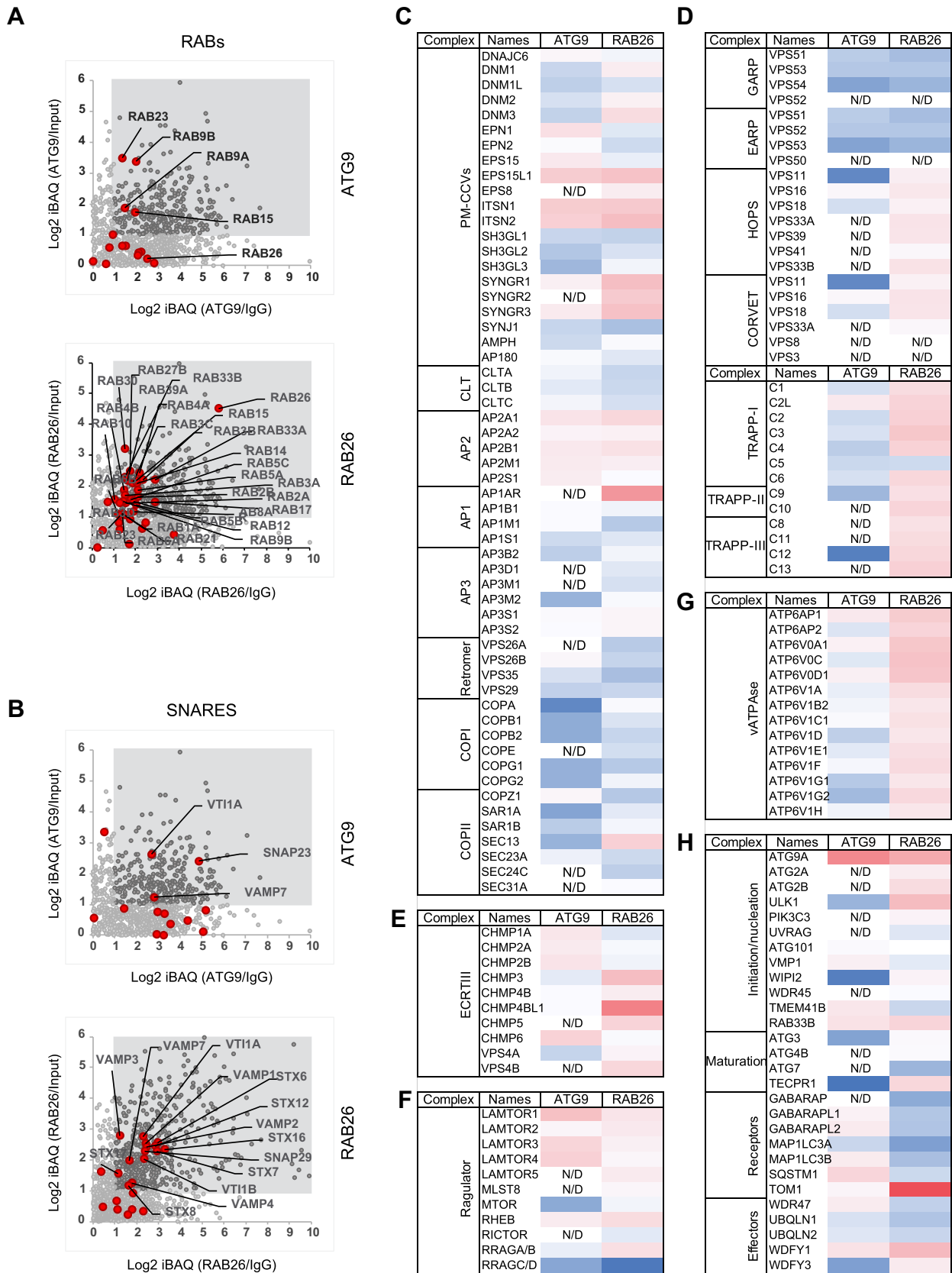


Figure 4. ATG9-containing vesicles are not enriched in proteins functioning in membrane traffic. (A and B) scatter plots showing enrichments of RAB GTPases and SNAREs (red dots) in the ATG9 and RAB26 vesicle proteomes (according to Figure 2)(C-H) heat map analysis showing the enrichment levels of coat proteins, tethering complexes, and other trafficking proteins in both proteomes. Enrichments were calculated as the average log₂ fold enrichment as described in the legend to Figure 3. Color code: red >0, and blue <0. See text for details.

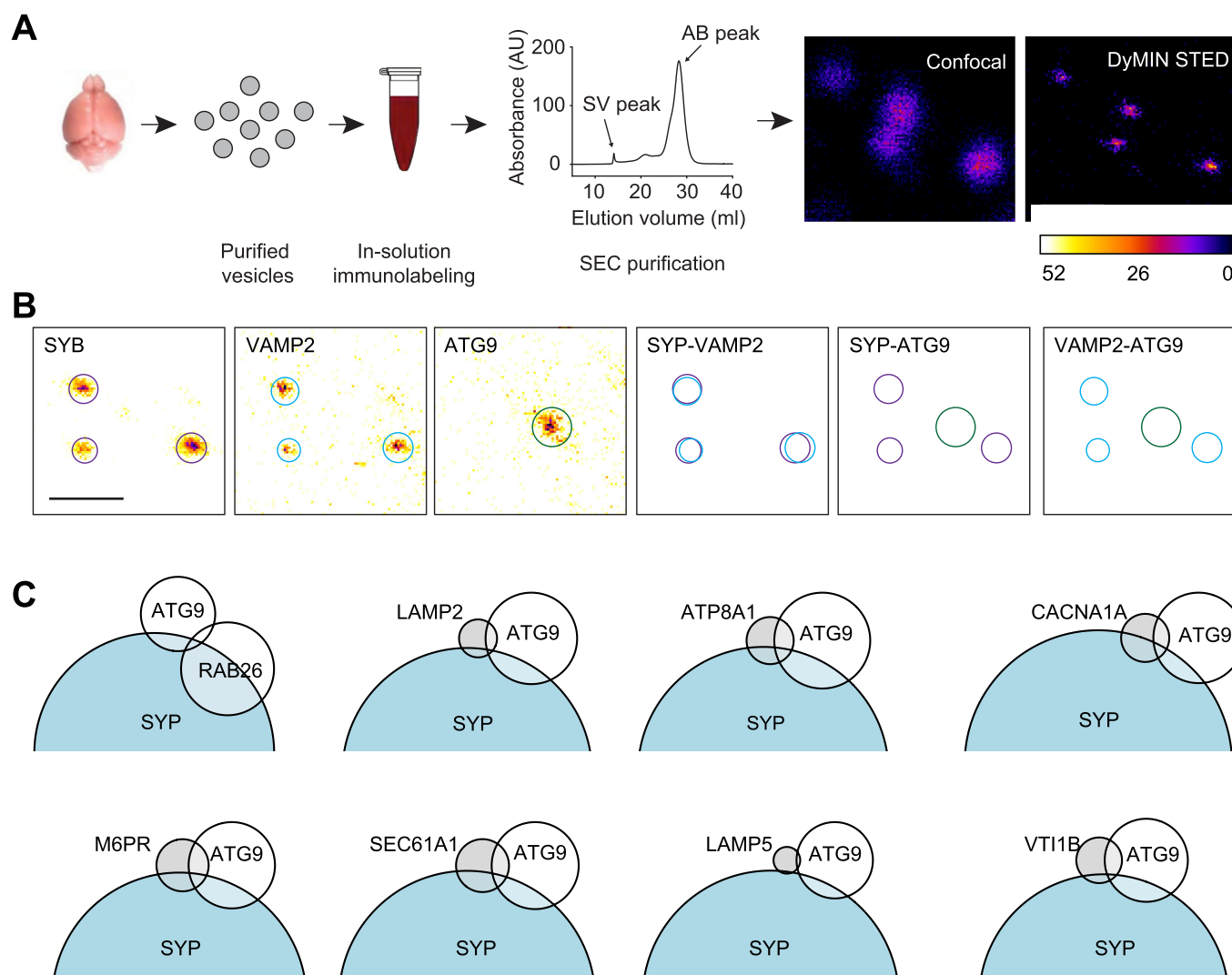


Figure 5. Single vesicle imaging by three-color DyMIN STED reveals sparse colocalization of ATG9 with markers for other intracellular organelles. (A) schematic illustration of the experiment: SVs were purified from rat brain, labeled in solution followed by removal of unbound antibody (AB) with size-exclusion chromatography and then imaged at single vesicle resolution using a DyMIN microscope (see Materials and Methods). Scale bar: 500 nm. (B) representative DyMIN STED images (inverse color map) of SVs for SYP, VAMP2/SYB2 and ATG9. Purple, magenta, and green circles portray the individual SV areas derived by a 2D Gaussian fit of SYP, VAMP2 and ATG9 puncta, respectively. Scale bar: 500 nm. (C) Venn diagrams displaying the degree of overlap between vesicles expressing ATG9, SYP, RAB26, and various membrane proteins specific for intracellular organelles, obtained by the three-color DyMIN STED imaging: the SNARE VTI1B, LAMP2, the aminophospholipid flippase ATP8A1, the P/Q type voltage-dependent calcium channel CACNA1A, M6PR, the protein translocon subunit SEC61A1, and LAMP5 (see text for details). The percentage of vesicles overlapping with ATG9 or SYP (in percent of ATG9 or SYP, respectively) were: RAB26; 6.5/49.3; LAMP2, 5.3/0.5; ATP8A1, 8.9/1.2; CACNA1A, 7.4/2.2; M6PR, 10.3/2.1; SEC61A1, 6.5/1.9; LAMP5; 0.2/0.02, VTI1B, 9.8/0.2. $n = 3$ experiments (involving independent vesicle preparations) for each combination; number of vesicles detected and analyzed in each experiment for SYP > 10,000; ATG9 > 1000; VTI1B = 761; LAMP2 = 631; ATP8A1 = 650; CACNA1A = 756; M6PR = 688; SEC61A1 = 867; LAMP5 = 467; RAB26 = 1247).

comprehensive analysis of ATG9 at the single vesicle level clearly identifies ATG9 as a distinct but highly heterogeneous vesicle pool at the synapse that, at least at the population level, is not related to SV recycling or to any other specific trafficking pathway.

To obtain more insight into the relationship between synaptic vesicles and ATG9-containing vesicles in different

neuronal compartments, we compared the distribution of ATG9 and the SV marker SYP in cultured primary hippocampal neurons using immunofluorescence detection (Figure 6A). When using standard confocal microscopy, a pixel-based colocalization correlation revealed that ATG9 largely overlaps with SYP in discrete puncta along the dendrites and albeit at modest levels, in non-synaptic regions

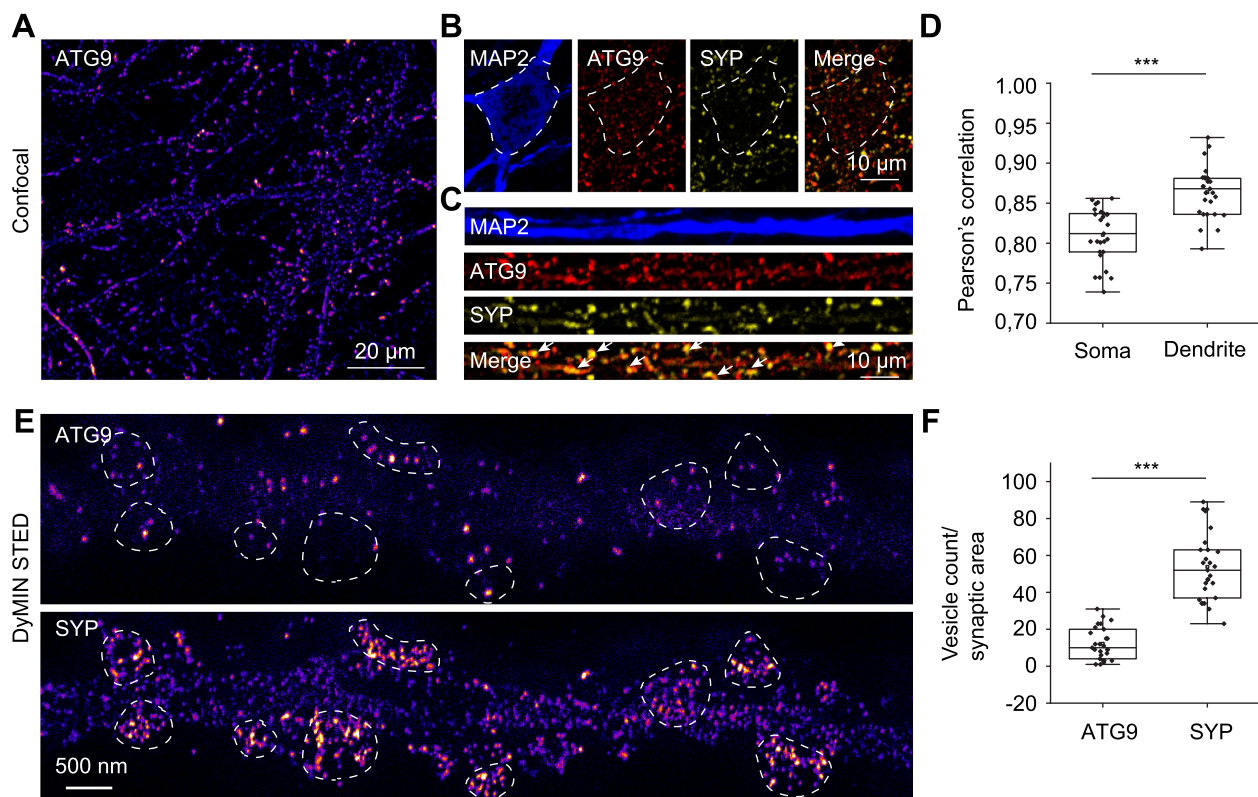


Figure 6. In cultured hippocampal neurons, ATG9 and SYP are both enriched in synapses but show only limited overlap. (A) representative confocal image showing an overview of ATG9 expression in cultured hippocampal neurons. Scale bar: 20 μm. (B) representative images of a soma region expressing ATG9, SYP and the merge of the two channels. Scale bar: 10 μm. (C) representative images of a straightened dendritic segment expressing ATG9, SYP and the merge of the two channels. White arrows indicate colocalized puncta. Scale bar: 10 μm. (D) box plot showing Pearson's colocalization correlation between ATG9 and SYP in the soma and dendritic regions (3 experiments). (E) representative two-color DyMIN STED images of dendritic segments showing ATG9 (top) and SYP (bottom) at single vesicle resolution, revealing that at this enhanced resolution co-localization is much lower than at the diffraction-limited resolution shown in C. The synaptic regions, defined by the AZ marker, PCLO, are encircled by white dotted lines. Scale bar: 500 nm. (F) box plot quantifying the number of ATG9 and SYP vesicles in individual synapses (27 synapses, 3 experiments).

where their overlap with SYP is less conspicuous (Figure 6B, C). This is indicated by the reduced overlap of ATG9-containing vesicles with SYP in the soma (average Pearson's correlation = 0.81 in the soma vs 0.86 in the dendrite) (Figures 6D).

To better compare the distributions of ATG9 and SYP in presynaptic boutons, we imaged both proteins using DyMIN STED (Figure 6E). PCLO (piccolo; a presynaptic cytomatrix protein) was used as active-zone (AZ) marker as a reference channel in the confocal mode in order to unequivocally identify presynaptic boutons along the dendrites (white dotted line). With this approach, individual vesicles could be at least partially resolved in two dimensions. At this enhanced resolution, we observed that overlap between the two proteins was limited, with the density of ATG9-containing vesicles (top panel) being conspicuously sparser than that of SYP vesicles (lower panel), as indicated in the box plot showing individual synapses with, in average, 10 and 50 vesicles containing ATG9 and SYP, respectively (Figure 6F).

To fully resolve individual vesicles inside presynaptic boutons in three dimensions, we imaged ATG9 and SYP by single molecule localization microscopy (SMLM) using 3D Minflux nanoscopy. Minflux is a recently developed SMLM method that requires minimal photon fluxes from the fluorophores for high localization precision [59,60]. We combined Minflux

with DNA PAINT labeling to allow for multiplexing and to reduce background noise ([61,62] see Materials and Methods). As above, PCLO was used as the reference channel for identifying presynaptic boutons and imaged in the confocal mode (Figure 7A). The enhanced resolution clearly revealed the presynaptic vesicles as clusters of fluorophores organized in 3D thus allowing us to fully resolve all labeled vesicles within presynaptic boutons (Figure 7B, and supplementary videos 1 and 2). The combination of Minflux and DNA PAINT dramatically improved the localization precision in both lateral and axial dimensions, with a localization precision of individual fluorophores between 1–3 nm in both axial and lateral dimensions (Figure 7C, see Materials and Methods), and it also improved the signal-to-noise ratio. For quantification, we identified individual vesicles with a machine learning algorithm that employed density-based cluster analysis (DBSCAN) and principal component analysis (PCA). With this approach, 450 ATG9-positive and 929 SYP-positive vesicles were counted in 20 individual synapses as shown in the box plot, combining data from four independent experiments (Figure 7D). There was no significant difference in the average diameter of ATG9 and SYP vesicles (Figure 7E,F). We next estimated the overlap between ATG9 and SYP vesicles. We again performed cluster analysis after merging both the localizations of ATG9 and SYP, and the clusters that contain

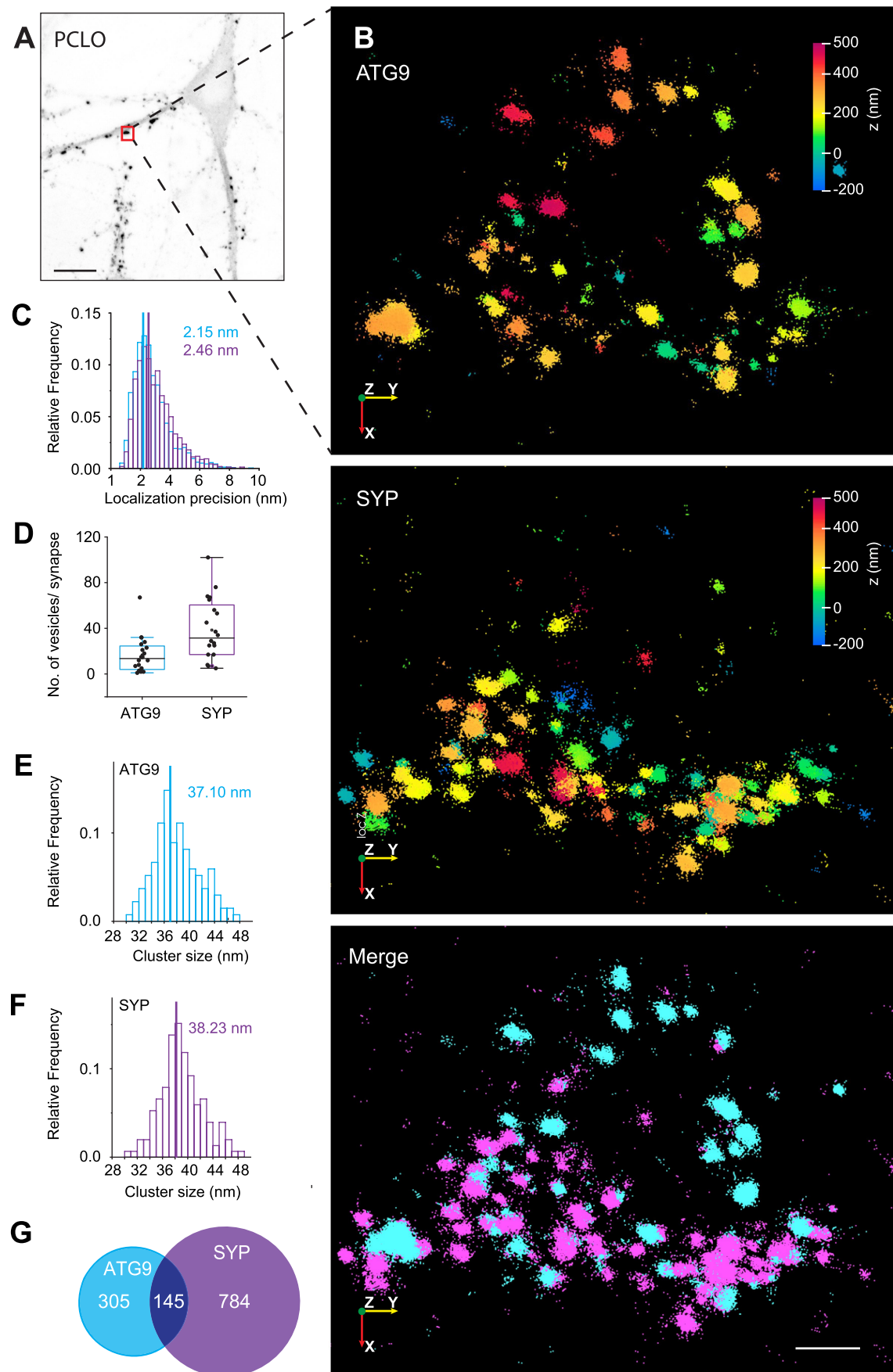


Figure 7. 3D resolution by Minflux nanoscopy of individual vesicles in synapses reveals that ATG9 and SYP vesicles represent distinct populations. (A) overview of the distribution of presynaptic regions in cultured hippocampal neurons, marked by the active zone protein PCLO. Scale bar: 10 μ m (B) Minflux raw images of the zoomed-in region from A (red box) showing 3D localizations of ATG9 (top) and SYP (middle) and the merge (bottom). While the top and middle images are color coded by the positions of the localizations in the z-axis, the bottom (merged) image shows distinct color codes for ATG9 (magenta) and SYP (purple) localizations.

localizations from both the channels were considered as vesicles containing both the proteins. Our analysis revealed ATG9 as a largely distinct vesicle pool at the presynapse that exhibits only limited overlap with the SVs containing SYP, as the vesicle population carrying both ATG9 and SYP accounted for only ~10% of all vesicles at the presynapse ((Figure 7G), and supplementary videos 1 and 2). Note that the percentage of ATG9-containing vesicles positive for SYP (~30%) is higher than that observed in our single vesicle imaging experiments. This may be due to a lower labeling efficiency of ATG9-containing vesicles in synapses, to a contribution of non-synaptic ATG9-containing vesicles devoid of SYP to our purified vesicle fraction, or to the presence of endosomes in synapses in which both proteins overlap and that are purified away during vesicle preparation. Despite these quantitative differences, the above experiments establish that ATG9-containing vesicles are enriched at the presynapse but represent a separate pool distinct from SVs.

Discussion

In the present study, we have thoroughly characterized neuronal ATG9-containing vesicles in order to better understand how these vesicles are connected to synaptic membrane trafficking pathways. Our findings show that ATG9-containing vesicles are concentrated in presynaptic nerve terminals where they represent a unique and morphologically rather homogeneous vesicle population. Overlap with proteins specific for other organelles is limited, showing that these vesicles are clearly distinct from synaptic vesicles, endosomes, or other presynaptic membrane compartments. Single vesicle analysis revealed multiple subpopulations that differ in their membrane composition, raising the possibility that synaptic ATG9-containing vesicles may originate from, or communicate with, a large diversity of intracellular compartments. On the other hand, they have conspicuously low levels of proteins required for membrane targeting, tethering, and fusion, and they also only contain low levels of the V-ATPase, distinguishing them from canonical trafficking vesicles.

ATG9, a conserved transmembrane protein essential for autophagy [63,64], follows the standard route of biogenesis for multispansing proteins, being synthesized in the rough endoplasmic reticulum and then delivered to the Golgi apparatus by vesicular traffic [65]. At the trans Golgi network (TGN), ATG9 is inserted into small vesicles, also known as ATG9-containing vesicles, that upon starvation-induced autophagy bud from the TGN and form clusters [18]. In non-neuronal cells, this “ATG9-compartment” appears to be highly dynamic [25]. In particular, ATG9 seems to shuttle between the Golgi apparatus, early/

recycling endosomes, and the plasma membrane using canonical trafficking pathways [66,67]. In a recent proteomic analysis of immuno-isolated ATG9-containing membranes from HEK cells, clear differences were observed between resting and starved conditions, with the latter depleted of Golgi proteins and enriched in phosphoinositide metabolizing enzymes [68]. Moreover, using BioID to identify proteins interacting with ATG9, both multisubunit tethering factors such as TRAPP, EARP, GARP, and exocyst, and the clathrin adaptor complexes AP-1, AP-3, and AP-4 were detected [69]. Together, these findings support the view of dynamic ATG9 recycling between the TGN, the plasma membrane, and the endosomal system [66,67]. Indeed, active cycling of ATG9-containing vesicles appears to be a prerequisite for functioning in autophagosome maturation since interference with ATG9-budding from recycling endosomes blocks autophagy [70].

In neurons, autophagosomes play a major role in synaptic homeostasis. They are mainly initiated in distal nerve endings and then mature during transport back toward the cell body [71] but the details of initial formation and growth are still unclear. Like in non-neuronal cells, ATG9-containing vesicles originate from the Trans Golgi Network [65]. However, in neurons the Golgi is confined to the somato-dendritic region, and thus ATG9-containing vesicles require anterograde axonal transport to reach synapses [29,72]. There are still large gaps in our understanding as to how exactly these vesicles mediate the delivery of membrane lipids, thus contributing to the growth of synaptic autophagosomes. For instance, it is unclear whether these vesicles are “one-shot” devices, thus requiring a constant supply by axonal transport of fresh, Golgi-derived, ATG9-containing vesicles for the growth of synaptic autophagosomes, or whether, after one round of lipid delivery, ATG9-containing vesicles recycle, e.g. by approaching other membranes in the synapse to scavenge lipids for additional rounds, and if so, whether such reloading involves fusion/budding of vesicles, lipid transfer at membrane contact sites, or even replenishment from soluble phospholipid carrier proteins.

Intriguingly, our proteomic analysis of synaptic ATG9-containing vesicles uncovered only low levels of trafficking proteins involved in both vesicle formation (budding) and vesicle consumption (tethering and fusion). The only exceptions are enrichments of the AP-2 complex and of plasma membrane resident proteins, in agreement with recent data showing that in *C. elegans* ATG9-containing vesicles undergo exo-endocytosis at synapses in an activity-dependent manner [28], and also of several PtdIns enzymes, particularly PI4K2A, PIP4K2A, PI4KA, PIP4P2/TMEM55A (see Figure S4). Also notable is the de-

Scale bar: 100 nm. (C) histogram showing the distribution of the combined (axial and lateral) localization precision (standard error of the mean) for ATG9 and SYP. (D) box plot quantifying the number of detected ATG9 and SYP vesicles per synapse ($n = 4$ independent experiments). (E and F) histogram showing the size distribution of ATG9 and SYP vesicles. (G) Venn diagram showing the overlap between ATG9 and SYP vesicles (32.2% of ATG9-containing vesicles carry SYP and 15.6% of SYP vesicles carry ATG9). The numbers in the diagram quantify ATG9 and SYP vesicles as determined by cluster analysis of individual fluorophores (see Materials and Methods).

enrichment of the V-ATPase (Figure 4G) suggesting that these vesicles do not acidify, clearly different from all post-Golgi trafficking vesicles. Particularly surprising is the lack of enrichment of most RABs and SNAREs, with the few ones being enriched known to function in different limbs of the post-Golgi trafficking pathways. This is in stark contrast to the RAB26 vesicles also present in the synapse, which resemble synaptic vesicles, are enriched in a large array of SNAREs and RAB GTPases [32], and contain proteins involved in endo-lysosomal trafficking such as the HOPS and TRAPP tethering complexes.

What do these results signify for the function of ATG9-containing vesicles in synapses? It is conceivable that under steady-state conditions synaptic ATG9-containing vesicles serve as a reserve pool for membrane lipids that is largely inactive with respect to trafficking (except of some exo-endocytotic cycling) waiting for being mobilized upon induction of autophagy to PAS initiation sites. On the other hand, it was previously suggested that neurons have a high basal autophagy flux [73,74], which is supported by some similarities between the synaptic ATG9-containing vesicles and starvation-induced ATG9-containing vesicles in non-neuronal cells. The latter scenario could explain the need for a local and fast regeneration of ATG9-containing vesicles in synapses [75], which may require a steady-state pool of ATG9-containing vesicles for buffering. In any case, considering the de-richment of trafficking proteins, it is conceivable that upon induction of synaptic autophagosome formation, the majority of ATG9-containing vesicles remain separate entities, recruiting and delivering membrane lipids by local contacts rather than by canonical vesicle traffic involving fusion and budding reactions.

Taken together, our results shed new light on membrane trafficking pathways inside presynaptic nerve terminals. In differentiated neurons, trafficking is dominated by the synaptic vesicle pathway [76]. Synaptic vesicles originate in the TGN, are transported by fast axonal transport to the synapse, where they undergo activity-dependent exo-endocytotic membrane recycling, being replenished with neurotransmitter by specific transporters during each cycle [77,78]. Endocytosis involves two distinct pathways, one involving clathrin-mediated endocytosis [79], and a second, ultrafast pathway involving re-capture of plasma membrane at a site adjacent to the active zone [80]. Recycling may involve early endosomal intermediates although the extent to which this is the case is still debated [81]. Less well characterized are the pathways functioning in the turnover of plasma membrane resident proteins such as receptors and ion channels [82]. These proteins are also inserted into post-Golgi trafficking vesicles and delivered by axonal transport to synapses where they fuse with the presynaptic plasma membrane, and they are also thought to pass through early endosomal intermediates after endocytosis [83]. While ATG9 generally appears to follow the same trafficking route, ATG9 is not only largely absent from synaptic vesicles but also from early endosomes as shown by its absence in RAB5A immuno-isolates, in contrast to SV proteins. Single particle imaging revealed a surprising diversity, with small and only partially

overlapping populations of ATG9-containing vesicles carrying protein residents of synaptic vesicles, the plasma membrane, endosomal/lysosomal compartments, and even the endoplasmic reticulum. The difference between ATG9-containing vesicles and synaptic vesicles, with limited overlap, was confirmed by superresolution imaging of synapses using Minflux nanoscopy, allowing for the first time to differentiate vesicle populations inside nerve terminals at the single vesicle level [84,85]. Intriguingly, our finding that ATG9-containing vesicles contain LC3 but lack ATG2 agrees with a recent study by Olivás, Wu [86] suggesting that ATG9-containing vesicles may represent “seed vesicles” in autophagosome formation, which precede the ATG2 state.

Presently, we can only speculate about the origin and significance of the surprising protein heterogeneity of ATG9-containing vesicles. Perhaps, formation of small ATG9-containing vesicles can be induced not only from the TGN but also from any of the other membranes participating in ATG9 trafficking. Thus, the heterogeneity would reflect “spillover” of diverse proteins incorporated into ATG9-containing vesicles during budding from these diverse precursor compartments, reflecting incomplete sorting, particularly if repetitive fusion/budding cycles are involved (see above). On the other hand, it is conceivable that the heterogeneity of ATG9-containing vesicles is already implemented by “dirty sorting” during their biogenesis at the TGN. Future work is required to clarify whether this heterogeneity has functional implications in autophagy, and whether these subpopulations exhibit differences in their trafficking routes.

After completion of this manuscript, a study was published in which tagged ATG9 and SYP were expressed in non-neuronal cells to show that the two proteins are sorted into different vesicles, with only SYP-containing vesicles segregating in liquid phases induced by the synaptic vesicle protein synapsin [87]. Moreover, proteomic analysis of the two vesicle populations revealed differences in the protein composition, with some similarities to our analysis of endogenous vesicles from synapses, despite the heterologous expression in non-neuronal cells. Taken together, these data lend strong support to our conclusion that despite their colocalization in synaptic nerve terminals and their ability to undergo exocytosis, synaptic vesicles and ATG9-containing vesicles represent structurally and functionally different vesicle populations.

Materials and Methods

Antibodies, plasmids, cell culture

For the subcellular fractionation and immuno-isolation experiments, antibodies specific for SYP (7.2; 101 011), RAB3A (42.2; 107111), RAB5A (621.3; 108011), RAB27B (168103), EEA1 (237002), VAMP2 (69.1; 104211), VAMP7 (232011), VTI1A (165003), SNAP23 (111202), were all from Synaptic Systems (SYSY). LC3B (ALX-803-081-C100) from ENZO, ATG2A (PD041) from MBL, PIP4K2A (D83C1; 5527) from Cell Signaling Technology. Whole IgG Sheep (Sh-003-Z) from Dianova, and the monoclonal rabbit ATG9 (ab108338) was purchased from Abcam.

For all DyMIN STED imaging experiments, antibodies for ATG9 (Abcam, ab108338), SYP (SYSY 101,011, 101308), VAMP2/SYB2 (SYSY 104,211), VTI1B (SYSY 164,005), LAMP2A (SYSY 437,005), ATP8A1 (ThermoFisher, PA5-62707), CACNA1A (SYSY 152,205), M6PR (Abcam, ab134153), SEC61A1 (ThermoFisher, PA5-21773), LAMP5 (SYSY 412,005), RAB26 (SYSY 269,011), PCLO/piccolo (SYSY 142,104) were used. In experiments, where usage of the same species antibodies was required, the primary antibodies were separately premixed with saturated concentrations of secondary nanobodies (Nanotag Biotechnologies, FluoTag[®]-X2 anti-Mouse IgG Kappa Light Chain- N1202, FluoTag[®]-X2 anti-Mouse IgG1-N2002 and FluoTag[®]-X2 anti-Rabbit IgG -N2402) and used.

For Minflux imaging experiments, antibodies for ATG9 (Abcam, ab108338), SYP (SYSY 101,011), PCLO/piccolo (SYSY 142,104) were used. For DNA PAINT imaging, anti-mouse, and anti-rabbit secondary nanobodies coupled to a single stranded oligonucleotide (Massive Photonics, docking strand, MASSIVE-sdAB 2-Plex) and complimentary oligonucleotides (imager strands) were used.

Isolation of synaptic vesicles

For the purification of synaptic vesicles from rat brain, subcellular fractionation was carried out as described [32,33]. In brief, synaptic vesicles were purified from rat brain homogenate by two consecutive differential centrifugation steps, yielding first a low-speed pellet P1 (enriched in cell debris and nuclei) and a supernatant S1 that was subjected to a second centrifugation yielding a pellet P2 (enriched in synaptosomes) and a supernatant S2. P2 was lysed by osmotic shock to release synaptic vesicles, followed by centrifugation to yield lysate pellet 1 (LP1) and a supernatant enriched in small vesicles and soluble proteins (lysate supernatant 1, LS1). LS1 was then subjected to ultracentrifugation, yielding lysate pellet 2 (LP2) containing small particles including vesicles, with the supernatant LS2 containing soluble proteins. LP2 was resuspended, and synaptic vesicles were purified by sucrose density gradient centrifugation followed by size exclusion chromatography with controlled pore glass beads where large membrane fractions (PK1) were separated from synaptic vesicles (SVs, or CPG-SVs).

Immuno-isolation of SVs was carried out as described [34] using the monoclonal antibody against SYP (7.2), RAB5A (621.3), RAB3A (42.2), and ATG9 ([EPR2450(2)]). Whole IgG from sheep was used as negative control. LS1 and LP2 were used as a starting material for the enrichment of ATG9 and RAB26 vesicles respectively. The immuno-isolates were eluted with 2X sample buffer without reducing agent and without boiling to avoid dissociation of the light chain and heavy chain of the antibody used for the immuno-isolation, thereby allowing detection of the RAB proteins that would otherwise migrate at the same size of the light chain.

Labeling of isolated SVs for imaging

Isolated SVs were immunolabeled as described recently [57]. Briefly, the SVs were incubated in a blocking solution (PBS;

ThermoFisher Scientific 10,010,023), pH 7.4, 5% normal goat serum (Invitrogen, 10000C) with constant rotation for 1 h at room temperature (RT), followed by the addition of saturating concentrations of primary antibodies (6 μ g/ml) and continued incubation for 1 h at RT. Next, the unbound, free antibodies were removed by size exclusion chromatography. To test the homogeneity and concentration of the labeled SVs, we performed Dynamic Lateral Scattering (DLS), further diluting the sample for immobilization on glass bottom dishes (4°C, 1 h). Afterwards, the SVs were fixed using 4% paraformaldehyde (PFA) for 5 min and washed thrice in PBS at an interval of 5 min. For secondary antibody labeling, the immobilized SVs were incubated in blocking solution for 30 min followed by secondary antibody incubation at a concentration of 8 mg/ml (a dilution of 1:250) for 1 h at RT. Afterwards, samples were washed thrice with PBS at an interval of 5 min. Finally, mounting media (Invitrogen, P36961) was applied on top of SVs and the images were typically acquired within 48 h of sample preparation. For three-color DyMIN STED imaging of purified SVs, primary antibodies raised against mouse, rabbit and guinea pig were used. In experiments, where usage of the same species antibodies was required, the primary antibodies were separately premixed with saturating concentrations of secondary nanobodies (Nanotag Biotechnologies, N2002, N1202, N2402).

DyMIN STED imaging

DyMIN STED nanoscopy was performed using a quad scanning STED microscope (Abberior Instruments, Göttingen, Germany) equipped with a UPlanSApo 100X/1.40 NA oil immersion objective (Olympus, Tokyo, Japan) and the optical set-up was described earlier (Heine et al., 2017). The pinhole was set to 1.0 Airy units and a pixel size of 15 nm was used. In three-color DyMIN STED imaging, a combination of Abberior Star Red (Ab.St.RED), Alexa Fluor 594 (AF594) and Alexa Fluor 488 (AF488) were used. Ab.St.RED was excited at 640 nm, AlexaFluor 594 at 561 nm and AF488 at 480 nm. Two different STED lasers (775 nm STED for Ab.ST.RED and AF594; 595 nm STED for AF488) were used. While imaging, the red spectrum signals were acquired first followed by the green-shifted signals to avoid bleaching of red fluorescence by the 595 nm STED laser. The fluorescence signal was detected using avalanche photo diodes with bandpass filters, and a gating of 0.75–8 ns was applied. Pixel dwell times of 10–20 ms were used. Each line was scanned 3 times and the signal was accumulated. The typical image size for purified SVs was 50 μ m².

Labeling of neurons using DNA PAINT

Hippocampal culture neurons (21 DIV), grown on 24-mm cover slips, were fixed using 4% PFA for 15 min. Then, the coverslips were washed twice, permeabilized (0.3% Triton X-100; ThermoFisher Scientific, A16046-AE) and blocked (5% normal goat serum) and incubated with primary antibodies for ATG9, SYP and PCLO/piccolo overnight. Next day, primary antibodies were removed, washed thrice, and secondary antibodies/nanobodies coupled to either

a fluorophore (anti-guinea pig-Alex Fluor 488; Invitrogen, A-11073) or specific single-stranded DNA docking strands (Site 1 and Site 2 for anti-mouse and anti-rabbit nanobodies, respectively, Massive Photonics, MASSIVE-SDAB 2-PLEX) were added and incubated for 1 h at room temperature. Finally, the samples were post-fixed using PFA, followed by a washing step using PBS.

Minflux imaging

Before imaging, each coverslip was incubated with fiducial gold beads (150 nm; BBI solutions, EM.GC20/7) for 5–10 min and the non-immobilized beads were removed by washing with PBS. The fiducial beads ensured nanometer scale stability of the sample during measurements by an active stabilization system that detected the 3D positions of the beads by a separated beamline and coupled with a galvanometer for real-time drift correction [88]. Next, single stranded DNA imager strands that are complimentary to one of the docking strands (Imager 1 or 2, Massive Photonics) was added to the sample and transferred to the microscope. Specific regions of interest (ROIs) ($<1.5 \mu\text{m} \times 1.5 \mu\text{m}$ area) were chosen using the PCLO channel and at least eight neighboring gold beads were assigned to each ROI as fiducial markers before starting the acquisition. Each ROI was imaged for 1 h for one imager strand followed by the other after a washing step. For sequential imaging with different imager strands, same gold beads were assigned to the ROI, and the drift during the washing steps, if any, was corrected in a registration step during the post processing of the images. Overall, the beads drift during the entire imaging duration was negligible with an average standard error less than 1 nm.

The optical setup contained three different illumination modalities provided through separate optical paths: (i) widefield excitation (488 nm, 560 nm and 640 nm), (ii) regularly focused excitation (560 nm or 642 nm) or focused activation (405 nm) and (iii) phase-modulated excitation (560 nm or 642 nm) leading to a 3D donut in the focal region. The scanning range of all beams was about $10 \times 10 \mu\text{m}^2$ in the lateral direction and 800 nm in the axial direction. A 1.4 numerical aperture oil immersion lens focused the excitation light into the sample and collected the fluorescence light. In contrast to the acquisition of fluorophore blinking events in regular SMLM, the transient binding of the imager strand with the docking strand acted as the blinking event. Microscopy data were acquired using Inspector software from Abberior Instruments.

Minflux image analysis

Data acquired by the Minflux system were analyzed using a modified custom code written in Python [89]. For two-color Minflux-PAINT images, spatial drift caused during the washing step was manually inspected for each measurement and corrected using the positions of the assigned fiducial beads. In Minflux, each “track” (tid) represents multiple detections (localizations) from single putative fluorophores. First, to filter spurious or background signals, we removed

the tracks that contained less than four localizations. Next, to detect if each track is indeed corresponding to single fluorophores, a cluster analysis was performed using Gaussian mixture model on localizations that belonged to the same track to split distinct clusters and a new list of tracks (tid2) was created. The localizations belonged to each tid2 were combined into “events”, which provided the localization precision (standard error of the mean) of single fluorophores. Furthermore, another cluster analysis of the “events” was performed using DBSCAN for a range of epsilon values (10 to 100 nm) and minimum points, MinPts (1 to 3). The results were examined for the size and distribution of clusters, allowing selection of appropriate epsilon value for specific proteins. For both ATG9 and SYP, an epsilon of 40 nm and MinPt 3 rendered a homogenous population of clusters with a diameter of ~ 38 nm, which is expected for small synaptic vesicles. To enhance stringency, clusters that contained only one event were excluded from the colocalization analysis. For two-color Minflux images, cluster analysis was performed after combining the events from both, ATG9 and SYP channels. Images were rendered using Paraview software.

Colocalization analysis

To determine vesicular colocalization in DyMIN STED imaging of purified SVs, we followed an “object based colocalization” strategy as described earlier [57,90]. In contrast to the regular pixel-based correlation analysis, object-based analysis considers the proximity of objects in space for calculation of colocalization. Any two/three proteins were considered as colocalized on the same vesicle if the distance between the centers of vesicles is less than 50 nm [57]. First, the individual images were median filtered using a radius of one pixel (15 nm) to remove single pixel background. Then, the coordinates of all the vesicles in the images were extracted using ThunderSTORM, an open source plug-in for Fiji [91]). Finally, the distance between the puncta in different images and the colocalization percentage were computed using a custom written R script. For colocalization analysis of the confocal images in culture neurons, images were background subtracted using the Rolling ball method with a radius of 50 pixels and colocalization correlation was performed using the Coloc 2 plugin in Fiji. Costes’ test ($p = 1$) was repeated 100 times to test statistical significance of the determined colocalization coefficients. For colocalization analysis of the DyMIN STED 2D images in culture neurons, the PCLO signal was segmented and the total number of ATG9 and SYP puncta in the segmented regions were determined by Particle analysis’ using Fiji.

For colocalization analysis of the Minflux 3D images, clusters that contained both ATG9 and SYP localizations were considered as vesicles containing both the proteins, and the clusters containing localizations from only one of the two proteins were labeled accordingly.

Electron microscopy

Morphological studies of ATG9-containing vesicles were performed as described in [14].

Sample preparation mass spectrometry-based proteomics

Proteins of immuno-isolated samples were resolved on NuPAGE 4–12% Bis-Tris gradient gels (ThermoFisher Scientific, NP0321BOX), stained with InstantBlue™ Coomassie Protein Stain (Expedeon, 194-ISB1L) and subjected to in-gel digestion with trypsin as previously described. Briefly, following Coomassie Brilliant Blue detection, all visible bands were excised, cut into approximately 1 mm² pieces, and subjected to in-gel reduction with 10 mM DTT, alkylation with 55 mM iodoacetamide, and overnight trypsinization (Promega, V5111). Tryptic peptides were extracted, dried, and reconstituted in 2% [v:v] acetonitrile and 0.05% [v:v] trifluoroacetic acid and subjected to liquid chromatography-tandem mass spectrometry (LC-MS/MS).

LC-MS/MS analysis

Peptides derived from three biological replicates were analyzed as technical duplicates on Q Exactive HF and HF-X Orbitrap mass spectrometers (Thermo Scientific), coupled to a Dionex UltiMate 3000 UHPLC system (Thermo Scientific) equipped with an in-house-packed C18 column (ReproSil-Pur 120 C18-AQ, 1.9- μ m pore size, 75- μ m inner diameter, 30-cm length; Dr. Maisch). Samples were separated using a 48-min gradient (start at 5% B, increase to 10% B in 3 min, followed by 10–45% B for 33 min, 90% B for 6 min, re-equilibration to 5% B for 6 min) at a flow rate of 300 nL/min, using 0.1% formic acid (v:v) as mobile phase A and 80% acetonitrile:0.08% formic acid (v:v) as mobile phase B. Eluting peptides were analyzed in positive mode using a data-dependent acquisition method (selecting the top 30 most abundant precursors for higher energy collision dissociation). MS1 spectra were acquired with a resolution of 60,000 FWHM in the Orbitrap covering a mass range of 350–1600 m/z , 100% automatic gain control (AGC) target (1×10^6), and 50 ms maximum injection time. Precursor ions were isolated using a 1.6 m/z isolation window, and a higher-energy collisional dissociation (HCD) of 30% was applied for fragmentation. Precursor ion charge state screening was enabled, all unassigned charge states were rejected, and only precursors with charge states from 2+ to 7+ were considered, and the dynamic exclusion was set to 25 s. MS2 spectra were acquired with a resolution of 15,000 FWHM, 100% AGC target (1×10^5), 60 ms maximum injection time.

Proteomic data analysis and visualization

Raw acquisition files were processed using the MaxQuant (MQ) software (version 1.6.5.0) [92,93] with the built-in Andromeda peptide search engine [94]. The spectra were searched against the complete *Rattus norvegicus* proteome sequence database generated from UniProt (UP000002494, accessed 29 March 2019, 21678 entries). Trypsin/P was set as digestion enzyme allowing up to two missed cleavage sites per peptide. Carbamidomethylated cysteines were set as fixed modifications, and oxidation of methionines and N-terminal acetylation were set as variable (a maximum number of five modifications per site was allowed). Maximum false discovery rate was kept at 1% at both peptide and protein levels. One

peptide with a minimum length of seven amino acids were defined as required for protein identification. The “Match between runs” option with default parameters was enabled to allow identifications to be transferred to non-sequenced MS features in other LC-MS runs. For intensity-based absolute quantification (iBAQ) [95], which normalizes each protein MS intensity by the corresponding number of identified peptides for any given protein, the “iBAQ” option was enabled.

Bioinformatic analysis was performed in the Perseus software environment (version 1.6.10.43) [96] using iBAQ values obtained through MaxQuant. Potential contaminants and identifications only by site or by reverse sequence were filtered out. iBAQ intensities were logarithmized (\log_2). The \log_2 iBAQ matrix was reduced based on valid values with a minimum of four out of six valid values in at least one group. Remaining missing values were imputed based on a normal distribution downshift of 1.4 and distribution width of 0.5. For 2D comparisons (i.e., to compare protein enrichment in ATG9 or RAB26 immuno-isolates with both control groups), the values in the previous iBAQ matrix were averaged for each group, and the averaged \log_2 iBAQ fold change (ATG9/Input) vs. \log_2 iBAQ fold change (ATG9/control IgG) and \log_2 iBAQ fold change (RAB26/Input) vs. \log_2 iBAQ fold change (RAB26/control IgG) were plotted. Proteins with \log_2 fold differences > 0 were defined to be enriched in ATG9/RAB26 immuno-isolates over control IgG and input.

Final matrices were exported from Perseus and further processed in Excel 2016 (Microsoft Office Package 2016) (see table S1 and S2). Organellar marker enrichment was determined based on \log_2 iBAQ values both vs control and vs input (e.g. cutoff of > 0.5 represents \log_2 iBAQ (ATG9/Input) > 0.5 as well as \log_2 iBAQ (ATG9/Control) > 0.5). The cutoff was increased in a stepwise manner from > 0 , 0.1, 0.2, 0.3, . . . , 1 to determine the relative dependency of organellar marker enrichment on cutoff stringency. Unless indicated otherwise a cutoff > 1 was selected all future analysis. Categorical annotation of proteins by biological function and/or subcellular localization was performed based on the following published scientific literature: SVs [36], mitochondria (Mito) [37]; Lysosomes, endosomes (EL) and peroxisomes (Px) [38]; plasma membrane (PM), endoplasmic reticulum (ER) and Golgi (GA) [39]. Molecular functions were attributed using Uniport and PANTHER databases.

Proportional Venn diagrams were generated in an online new R package called eulerr (<http://eulerr.co/>). The Venn diagrams were undertaken using Adobe Illustrator 2022. Exploratory data analysis was performed in R 4.1.2 (<https://www.npackd.org/p/r/4.1.2>) and final plots were prepared for display using the packages “ggplot2” [97] and “cowplot” using R package version 1.1.1. (<https://CRAN.R-project.org/package=cowplot>). All data was assembled for display in Adobe Illustrator (Adobe Systems).

Human subjects or animals

There are no human or animal behavioral experiments performed for this study. The number of rats used for the vesicle

and neuronal preparations are given in the specific Materials and Methods section.

Statistical analyses

Details on the statistical approaches used are given in the figure legends and Materials and Methods section. For all statistical tests, sample size is given in the figure legend. All imaging experiments were repeated at least three times using different biological and technical samples.

Acknowledgements

We thank Dr. Cornelius Schneider for the useful suggestions and constructive discussion. We thank Dr. Antonio Politi and Dr. Jan Keller-Findeison (MPI) for writing the initial code for the Minflux data analysis. We also thank Isabelle Jansen (Abberior Instruments) for the assistance in Minflux data acquisition. We thank Sabine König, Monika Raabe, Ralf Pflanz and Uwe Plessmann for help in mass spectrometry. We thank Brigitte Barg-Kues for the technical assistance and Sigrid Schmidt for the preparation of neuronal cultures.

Disclosure statement

No potential conflict of interest was reported by the author(s).

Funding

The work was supported by the Deutsche Forschungsgemeinschaft [SFB1286].

Data availability statement

The python code used in this study for Minflux imaging data analysis is available in the GitHub link <https://github.com/ssamban1/Minflux>. The mass spectrometry proteomics data have been deposited to the ProteomeXchange Consortium via the PRIDE [98] partner repository with the dataset identifier PXD041702

ORCID

Reinhard Jahn  <http://orcid.org/0000-0003-1542-3498>

References

- [1] Sudhof TC. The synaptic vesicle cycle. *Annu Rev Neurosci.* 2004;27(1):509–547. doi: 10.1146/annurev.neuro.26.041002.131412
- [2] Jahn R, Fasshauer D. Molecular machines governing exocytosis of synaptic vesicles. *Nature.* 2012;490(7419):201–207. doi: 10.1038/nature11320
- [3] Brunger AT, Choi UB, Lai Y, et al. The pre-synaptic fusion machinery. *Curr Opin Struct Biol.* 2019;54:179–188. doi: 10.1016/j.sbi.2019.03.007
- [4] Alvarez-Castelao B, Schuman EM. The regulation of synaptic protein turnover. *J Biol Chem.* 2015;290(48):28623–28630. doi: 10.1074/jbc.R115.657130
- [5] Truckenbrodt S, Viplav A, Jähne S, et al. Newly produced synaptic vesicle proteins are preferentially used in synaptic transmission. *EMBO J.* 2018;37(15):37(15). doi: 10.15252/embj.201798044
- [6] Jähne S, Mikulasch F, Heuer GHG, et al. Presynaptic activity and protein turnover are correlated at the single-synapse level. *Cell Rep.* 2021;34(11):108841. doi: 10.1016/j.celrep.2021.108841
- [7] Gundelfinger ED, Karpova A, Pielot R, et al. Organization of presynaptic autophagy-related processes. *Front Synaptic Neurosci.* 2022;14:829354. doi: 10.3389/fnsyn.2022.829354
- [8] Soykan T, Haucke V, Kuijpers M. Mechanism of synaptic protein turnover and its regulation by neuronal activity. *Curr Opin Neurobiol.* 2021;69:76–83. doi: 10.1016/j.conb.2021.02.006
- [9] Kulkarni VV, Stempel MH, Anand A, et al. Retrograde axonal autophagy and endocytic pathways are parallel and separate in neurons. *J Neurosci.* 2022;42(45):8524–8541. doi: 10.1523/JNEUROSCI.1292-22.2022
- [10] Vietri M, Radulovic M, Stenmark H. The many functions of ESCRTs. *Nat Rev Mol Cell Biol.* 2020;21(1):25–42. doi: 10.1038/s41580-019-0177-4
- [11] Von Bartheld CS, Altick AL. Multivesicular bodies in neurons: distribution, protein content, and trafficking functions. *Prog Neurobiol.* 2011;93(3):313–340. doi: 10.1016/j.pneurobio.2011.01.003
- [12] Mercer TJ, Gubas A, Tooze SA. A molecular perspective of mammalian autophagosome biogenesis. *J Biol Chem.* 2018;293(15):5386–5395. doi: 10.1074/jbc.R117.810366
- [13] Stavoe AKH, Holzbaur ELF. Autophagy in neurons. *Annu Rev Cell Dev Biol.* 2019;35:477–500. doi: 10.1146/annurev-cellbio-100818-125242
- [14] Binotti B, Pavlos NJ, Riedel D, et al. The GTPase Rab26 links synaptic vesicles to the autophagy pathway. *Elife.* 2015;4:e05597. doi: 10.7554/eLife.05597
- [15] Dong W, He B, Qian H, et al. RAB26-dependent autophagy protects adherens junctional integrity in acute lung injury. *Autophagy.* 2018;14(10):1677–1692. doi: 10.1080/15548627.2018.1476811
- [16] Luningschror P, Binotti B, Dombert B, et al. Plekhg5-regulated autophagy of synaptic vesicles reveals a pathogenic mechanism in motoneuron disease. *Nat Commun.* 2017;8(1):678. doi: 10.1038/s41467-017-00689-z
- [17] Barz S, Kriegenburg F, Sánchez-Martín P, et al. Small but mighty: Atg8s and rabs in membrane dynamics during autophagy. *Biochim Biophys Acta, Mol Cell Res.* 2021;1868(9):119064. doi: 10.1016/j.bbamcr.2021.119064
- [18] Nishimura T, Tooze SA. Emerging roles of ATG proteins and membrane lipids in autophagosome formation. *Cell Discov.* 2020;6(1):32. doi: 10.1038/s41421-020-0161-3
- [19] Grasso D, Renna FJ, Vaccaro MI. Initial steps in mammalian autophagosome biogenesis. *Front Cell Dev Biol.* 2018;6:146. doi: 10.3389/fcell.2018.00146
- [20] Matoba K, Kotani T, Tsutsumi A, et al. Atg9 is a lipid scramblase that mediates autophagosomal membrane expansion. *Nat Struct Mol Biol.* 2020;27(12):1185–1193. doi: 10.1038/s41594-020-00518-w
- [21] Maeda S, Yamamoto H, Kinch LN, et al. Structure, lipid scrambling activity and role in autophagosome formation of ATG9A. *Nat Struct Mol Biol.* 2020;27(12):1194–1201. doi: 10.1038/s41594-020-00520-2
- [22] Guardia CM, Tan X-F, Lian T, et al. Structure of human ATG9A, the only transmembrane protein of the core autophagy machinery. *Cell Rep.* 2020;31(13):107837. doi: 10.1016/j.celrep.2020.107837
- [23] Osawa T, Kotani T, Kawaoka T, et al. Atg2 mediates direct lipid transfer between membranes for autophagosome formation. *Nat Struct Mol Biol.* 2019;26(4):281–288. doi: 10.1038/s41594-019-0203-4
- [24] Tang Z, Takahashi Y, He H, et al. TOM40 targets Atg2 to mitochondria-associated ER membranes for phagophore expansion. *Cell Rep.* 2019;28(7):1744–1757 e5. doi: 10.1016/j.celrep.2019.07.036
- [25] Orsi A, Razi M, Dooley HC, et al. Dynamic and transient interactions of Atg9 with autophagosomes, but not membrane integration, are required for autophagy. *Mol Biol Cell.* 2012;23(10):1860–1873. doi: 10.1091/mbc.e11-09-0746
- [26] Karanasios E, Walker SA, Okkenhaug H, et al. Autophagy initiation by ULK complex assembly on ER tubulovesicular regions marked by ATG9 vesicles. *Nat Commun.* 2016;7(1):12420. doi: 10.1038/ncomms12420

- [27] Gomez-Sanchez R, Tooze SA, Reggiori F. Membrane supply and remodeling during autophagosome biogenesis. *Curr Opin Cell Biol.* 2021;71:112–119. doi: [10.1016/j.ceb.2021.02.001](https://doi.org/10.1016/j.ceb.2021.02.001)
- [28] Yang S, Park D, Manning L, et al. Presynaptic autophagy is coupled to the synaptic vesicle cycle via ATG-9. *Neuron.* 2022;110(5):824–840 e10. doi: [10.1016/j.neuron.2021.12.031](https://doi.org/10.1016/j.neuron.2021.12.031)
- [29] Stavoe AK, Hill S, Hall D, et al. KIF1A/UNC-104 transports ATG-9 to regulate neurodevelopment and autophagy at synapses. *Dev Cell.* 2016;38(2):171–185. doi: [10.1016/j.devcel.2016.06.012](https://doi.org/10.1016/j.devcel.2016.06.012)
- [30] Maday S, Holzbaur EL. Autophagosome biogenesis in primary neurons follows an ordered and spatially regulated pathway. *Dev Cell.* 2014;30(1):71–85. doi: [10.1016/j.devcel.2014.06.001](https://doi.org/10.1016/j.devcel.2014.06.001)
- [31] Boyken J, Grønborg M, Riedel D, et al. Molecular profiling of synaptic vesicle docking sites reveals novel proteins but few differences between glutamatergic and GABAergic synapses. *Neuron.* 2013;78(2):285–297. doi: [10.1016/j.neuron.2013.02.027](https://doi.org/10.1016/j.neuron.2013.02.027)
- [32] Takamori S, Holt M, Stenius K, et al. Molecular anatomy of a trafficking organelle. *Cell.* 2006;127(4):831–846. doi: [10.1016/j.cell.2006.10.030](https://doi.org/10.1016/j.cell.2006.10.030)
- [33] Huttner WB, Schiebler W, Greengard P, et al. Synapsin I (protein I), a nerve terminal-specific phosphoprotein. III. Its association with synaptic vesicles studied in a highly purified synaptic vesicle preparation. *J Cell Bio.* 1983;96(5):1374–1388. doi: [10.1083/jcb.96.5.1374](https://doi.org/10.1083/jcb.96.5.1374)
- [34] Fischer von Mollard G, Stahl B, Walch-Solimena C, et al. Localization of Rab5 to synaptic vesicles identifies endosomal intermediate in synaptic vesicle recycling pathway. *Eur J Cell Biol.* 1994;65(2):319–326.
- [35] Stenmark H. Rab GTPases as coordinators of vesicle traffic. *Nat Rev Mol Cell Biol.* 2009;10(8):513–525. doi: [10.1038/nrm2728](https://doi.org/10.1038/nrm2728)
- [36] Taoufiq Z, Ninov M, Villar-Briones A, et al. Hidden proteome of synaptic vesicles in the mammalian brain. *Proc Natl Acad Sci U S A.* 2020;117(52):33586–33596. doi: [10.1073/pnas.2011870117](https://doi.org/10.1073/pnas.2011870117)
- [37] Morgenstern M, Peikert CD, Lübbert P, et al. Quantitative high-confidence human mitochondrial proteome and its dynamics in cellular context. *Cell Metab.* 2021;33(12):2464–2483 e18. doi: [10.1016/j.cmet.2021.11.001](https://doi.org/10.1016/j.cmet.2021.11.001)
- [38] Eapen VV, Swarup S, Hoyer MJ, et al. Quantitative proteomics reveals the selectivity of ubiquitin-binding autophagy receptors in the turnover of damaged lysosomes by lysophagy. *Elife.* 2021;10:10. doi: [10.7554/eLife.72328](https://doi.org/10.7554/eLife.72328)
- [39] Geladaki A, Kočevár Britovšek N, Breckels LM, et al. Combining LOPIT with differential ultracentrifugation for high-resolution spatial proteomics. *Nat Commun.* 2019;10(1):331. doi: [10.1038/s41467-018-08191-w](https://doi.org/10.1038/s41467-018-08191-w)
- [40] Shin JJH, Crook OM, Borgeaud AC, et al. Spatial proteomics defines the content of trafficking vesicles captured by golgin tethers. *Nat Commun.* 2020;11(1):5987. doi: [10.1038/s41467-020-19840-4](https://doi.org/10.1038/s41467-020-19840-4)
- [41] Jin RU, Mills JC. RAB26 coordinates lysosome traffic and mitochondrial localization. *J Cell Sci.* 2014;127(Pt 5):1018–1032. doi: [10.1242/jcs.138776](https://doi.org/10.1242/jcs.138776)
- [42] Riederer MA, Soldati T, Shapiro AD, et al. Lysosome biogenesis requires Rab9 function and receptor recycling from endosomes to the trans-Golgi network. *J Cell Bio.* 1994;125(3):573–582. doi: [10.1083/jcb.125.3.573](https://doi.org/10.1083/jcb.125.3.573)
- [43] Kucera A, Borg Distefano M, Berg-Larsen A, et al. Spatiotemporal resolution of Rab9 and CI-MPR dynamics in the endocytic pathway. *Traffic.* 2016;17(3):211–229. doi: [10.1111/tra.12357](https://doi.org/10.1111/tra.12357)
- [44] Evans TM, Ferguson C, Wainwright, BJ, et al. Rab23, a negative regulator of hedgehog signaling, localizes to the plasma membrane and the endocytic pathway. *Traffic.* 2003;4(12):869–884. doi: [10.1046/j.1600-0854.2003.00141.x](https://doi.org/10.1046/j.1600-0854.2003.00141.x)
- [45] Pavlos NJ, Grønborg M, Riedel D, et al. Quantitative analysis of synaptic vesicle rabs uncovers distinct yet overlapping roles for Rab3a and Rab27b in ca²⁺-triggered exocytosis. *J Neurosci.* 2010;30(40):13441–13453. doi: [10.1523/JNEUROSCI.0907-10.2010](https://doi.org/10.1523/JNEUROSCI.0907-10.2010)
- [46] Popova NV, Deyev IE, Petrenko AG. Clathrin-mediated endocytosis and adaptor proteins. *Acta Naturae.* 2013;5(3):62–73. doi: [10.32607/20758251-2013-5-3-62-73](https://doi.org/10.32607/20758251-2013-5-3-62-73)
- [47] Milosevic I. Revisiting the role of clathrin-mediated Endocytosis in synaptic vesicle recycling. *Front Cell Neurosci.* 2018;12:27. doi: [10.3389/fncel.2018.00027](https://doi.org/10.3389/fncel.2018.00027)
- [48] Schroeter S, Beckmann S, Schmitt HD. Coat/Tether interactions-exception or rule? *Front Cell Dev Biol.* 2016;4:44. doi: [10.3389/fcell.2016.00044](https://doi.org/10.3389/fcell.2016.00044)
- [49] Aridor M. A tango for coats and membranes: new insights into ER-to-Golgi traffic. *Cell Rep.* 2022;38(3):110258. doi: [10.1016/j.celrep.2021.110258](https://doi.org/10.1016/j.celrep.2021.110258)
- [50] Schellmann S, Pimpl P. Coats of endosomal protein sorting: retromer and ESCRT. *Curr Opin Plant Biol.* 2009;12(6):670–676. doi: [10.1016/j.pbi.2009.09.005](https://doi.org/10.1016/j.pbi.2009.09.005)
- [51] Solinger JA, Spang A. Tethering complexes in the endocytic pathway: CORVET and HOPS. *FEBS J.* 2013;280(12):2743–2757. doi: [10.1111/febs.12151](https://doi.org/10.1111/febs.12151)
- [52] Balderhaar HJ, Ungerermann C. CORVET and HOPS tethering complexes - coordinators of endosome and lysosome fusion. *J Cell Sci.* 2013;126(Pt 6):1307–1316. doi: [10.1242/jcs.107805](https://doi.org/10.1242/jcs.107805)
- [53] Kim JJ, Lipatova Z, Segev N. TRAPP complexes in secretion and autophagy. *Front Cell Dev Biol.* 2016;4:20. doi: [10.3389/fcell.2016.00020](https://doi.org/10.3389/fcell.2016.00020)
- [54] Sacher M, Shahrzad N, Kamel H, et al. Trappopathies: an emerging set of disorders linked to variations in the genes encoding transport protein particle (TRAPP)-associated proteins. *Traffic.* 2019;20(1):5–26. doi: [10.1111/tra.12615](https://doi.org/10.1111/tra.12615)
- [55] Ballabio A, Bonifacino JS. Lysosomes as dynamic regulators of cell and organismal homeostasis. *Nat Rev Mol Cell Biol.* 2020;21(2):101–118. doi: [10.1038/s41580-019-0185-4](https://doi.org/10.1038/s41580-019-0185-4)
- [56] Song Q, Meng B, Xu H, et al. The emerging roles of vacuolar-type ATPase-dependent lysosomal acidification in neurodegenerative diseases. *Transl Neurodegener.* 2020;9(1):17. doi: [10.1186/s40035-020-00196-0](https://doi.org/10.1186/s40035-020-00196-0)
- [57] Upmanyu N, Jin J, Emde HVD, et al. Colocalization of different neurotransmitter transporters on synaptic vesicles is sparse except for VGLUT1 and ZnT3. *Neuron.* 2022;110(9):1483–1497 e7. doi: [10.1016/j.neuron.2022.02.008](https://doi.org/10.1016/j.neuron.2022.02.008)
- [58] Heine J, Reuss M, Harke B, et al. Adaptive-illumination STED nanoscopy. *Proc Natl Acad Sci U S A.* 2017;114(37):9797–9802. doi: [10.1073/pnas.1708304114](https://doi.org/10.1073/pnas.1708304114)
- [59] Balzarotti F, Eilers Y, Gwosch KC, et al. Nanometer resolution imaging and tracking of fluorescent molecules with minimal photon fluxes. *Science.* 2017;355(6325):606–612. doi: [10.1126/science.aak9913](https://doi.org/10.1126/science.aak9913)
- [60] Gwosch KC, Pape JK, Balzarotti F, et al. MINFLUX nanoscopy delivers 3D multicolor nanometer resolution in cells. *Nat Methods.* 2020;17(2):217–224. doi: [10.1038/s41592-019-0688-0](https://doi.org/10.1038/s41592-019-0688-0)
- [61] Jungmann R, Avendaño MS, Woehrstein JB, et al. Multiplexed 3D cellular super-resolution imaging with DNA-PAINT and exchange-PAINT. *Nat Methods.* 2014;11(3):313–318. doi: [10.1038/nmeth.2835](https://doi.org/10.1038/nmeth.2835)
- [62] Ostersehl LM, Jans DC, Wittek A, et al. DNA-PAINT MINFLUX nanoscopy. *Nat Methods.* 2022;19(9):1072–1075. doi: [10.1038/s41592-022-01577-1](https://doi.org/10.1038/s41592-022-01577-1)
- [63] Noda T, Kim J, Huang W-P, et al. Apg9p/Cvt7p is an integral membrane protein required for transport vesicle formation in the cvt and autophagy pathways. *J Cell Bio.* 2000;148(3):465–480. doi: [10.1083/jcb.148.3.465](https://doi.org/10.1083/jcb.148.3.465)
- [64] Webber JL, Tooze SA. New insights into the function of Atg9. *FEBS Lett.* 2010;584(7):1319–1326. doi: [10.1016/j.febslet.2010.01.020](https://doi.org/10.1016/j.febslet.2010.01.020)
- [65] De Tito S, Hervás JH, van Vliet AR, et al. The Golgi as an assembly line to the autophagosome. *Trends Biochem Sci.* 2020;45(6):484–496. doi: [10.1016/j.tibs.2020.03.010](https://doi.org/10.1016/j.tibs.2020.03.010)
- [66] Mattera R, Park SY, De Pace R, et al. AP-4 mediates export of ATG9A from the trans-Golgi network to promote autophagosome

- formation. *Proc Natl Acad Sci U S A*. 2017;114(50):E10697–E10706. doi: [10.1073/pnas.1717327114](https://doi.org/10.1073/pnas.1717327114)
- [67] Davies AK, Itzhak DN, Edgar JR, et al. AP-4 vesicles contribute to spatial control of autophagy via RUSC-dependent peripheral delivery of ATG9A. *Nat Commun*. 2018;9(1):3958. doi: [10.1038/s41467-018-06172-7](https://doi.org/10.1038/s41467-018-06172-7)
- [68] Judith D, Jefferies HBJ, Boeing S, et al. ATG9A shapes the forming autophagosome through Arfaptin 2 and phosphatidylinositol 4-kinase III β . *J Cell Bio*. 2019;218(5):1634–1652. doi: [10.1083/jcb.201901115](https://doi.org/10.1083/jcb.201901115)
- [69] Kannagara AR, Poole DM, McEwan CM, et al. BioID reveals an ATG9A interaction with ATG13-ATG101 in the degradation of p62/SQSTM1-ubiquitin clusters. *EMBO Rep*. 2021;22(10):e51136. doi: [10.15252/embr.202051136](https://doi.org/10.15252/embr.202051136)
- [70] De Pace R, Skirzewski M, Damme M, et al. Altered distribution of ATG9A and accumulation of axonal aggregates in neurons from a mouse model of AP-4 deficiency syndrome. *PLoS Genet*. 2018;14(4):e1007363. doi: [10.1371/journal.pgen.1007363](https://doi.org/10.1371/journal.pgen.1007363)
- [71] Maday S, Wallace KE, Holzbaur EL. Autophagosomes initiate distally and mature during transport toward the cell soma in primary neurons. *J Cell Bio*. 2012;196(4):407–417. doi: [10.1083/jcb.201106120](https://doi.org/10.1083/jcb.201106120)
- [72] Hill SE, Colon-Ramos DA. The journey of the synaptic autophagosome: a Cell biological perspective. *Neuron*. 2020;105(6):961–973. doi: [10.1016/j.neuron.2020.01.018](https://doi.org/10.1016/j.neuron.2020.01.018)
- [73] Valencia M, Kim SR, Jang Y, et al. Neuronal autophagy: characteristic features and roles in neuronal pathophysiology. *Biomol Ther*. 2021;29(6):605–614. doi: [10.4062/biomolther.2021.012](https://doi.org/10.4062/biomolther.2021.012)
- [74] Ariosa AR, Klionsky DJ. Autophagy core machinery: overcoming spatial barriers in neurons. *J Mol Med (Berl)*. 2016;94(11):1217–1227. doi: [10.1007/s00109-016-1461-9](https://doi.org/10.1007/s00109-016-1461-9)
- [75] Maday S, Holzbaur EL. Compartment-specific Regulation of autophagy in primary neurons. *J Neurosci*. 2016;36(22):5933–5945. doi: [10.1523/JNEUROSCI.4401-15.2016](https://doi.org/10.1523/JNEUROSCI.4401-15.2016)
- [76] Wilhelm BG, Mandad S, Truckenbrodt S, et al. Composition of isolated synaptic boutons reveals the amounts of vesicle trafficking proteins. *Science*. 2014;344(6187):1023–1028. doi: [10.1126/science.1252884](https://doi.org/10.1126/science.1252884)
- [77] Rizzoli SO. Synaptic vesicle recycling: steps and principles. *EMBO J*. 2014;33(8):788–822. doi: [10.1002/embj.201386357](https://doi.org/10.1002/embj.201386357)
- [78] Anne C, Gasnier B. Vesicular neurotransmitter transporters: mechanistic aspects. *Curr Top Membr*. 2014;73:149–174.
- [79] Granseth B, Odermatt B, Royle S, et al. Clathrin-mediated endocytosis is the dominant mechanism of vesicle retrieval at hippocampal synapses. *Neuron*. 2006;51(6):773–786. doi: [10.1016/j.neuron.2006.08.029](https://doi.org/10.1016/j.neuron.2006.08.029)
- [80] Watanabe S, Rost BR, Camacho-Pérez M, et al. Ultrafast endocytosis at mouse hippocampal synapses. *Nature*. 2013;504(7479):242–247. doi: [10.1038/nature12809](https://doi.org/10.1038/nature12809)
- [81] Saheki Y, De Camilli P. Synaptic vesicle endocytosis. *Cold Spring Harb Perspect Biol*. 2012;4(9):a005645. doi: [10.1101/cshperspect.a005645](https://doi.org/10.1101/cshperspect.a005645)
- [82] Jin EJ, Kiral FR, Hiesinger PR. The where, what, and when of membrane protein degradation in neurons. *Dev Neurobiol*. 2018;78(3):283–297. doi: [10.1002/dneu.22534](https://doi.org/10.1002/dneu.22534)
- [83] Maas C, Torres VI, Altmann WD, et al. Formation of Golgi-derived active zone precursor vesicles. *J Neurosci*. 2012;32(32):11095–11108. doi: [10.1523/JNEUROSCI.0195-12.2012](https://doi.org/10.1523/JNEUROSCI.0195-12.2012)
- [84] Hua Z, Leal-Ortiz S, Foss S, et al. V-SNARE composition distinguishes synaptic vesicle pools. *Neuron*. 2011;71(3):474–487. doi: [10.1016/j.neuron.2011.06.010](https://doi.org/10.1016/j.neuron.2011.06.010)
- [85] Rizzoli SO, Betz WJ. Synaptic vesicle pools. *Nat Rev Neurosci*. 2005;6(1):57–69. doi: [10.1038/nrn1583](https://doi.org/10.1038/nrn1583)
- [86] Olivás TJ, Wu Y, Yu S, et al. ATG9 vesicles comprise the seed membrane of mammalian autophagosomes. *J Cell Bio*. 2023;222(7):222(7). doi: [10.1083/jcb.202208088](https://doi.org/10.1083/jcb.202208088)
- [87] Park D, Wu Y, Wang X, et al. Synaptic vesicle proteins and ATG9A self-organize in distinct vesicle phases within synapsin condensates. *Nat Commun*. 2023;14(1):455. doi: [10.1038/s41467-023-36081-3](https://doi.org/10.1038/s41467-023-36081-3)
- [88] Schmidt R, Weihs T, Wurm CA, et al. MINFLUX nanometer-scale 3D imaging and microsecond-range tracking on a common fluorescence microscope. *Nat Commun*. 2021;12(1):1478. doi: [10.1038/s41467-021-21652-z](https://doi.org/10.1038/s41467-021-21652-z)
- [89] Pape JK, Stephan T, Balzarotti F, et al. Multicolor 3D MINFLUX nanoscopy of mitochondrial MICOS proteins. *Proc Natl Acad Sci U S A*. 2020;117(34):20607–20614. doi: [10.1073/pnas.2009364117](https://doi.org/10.1073/pnas.2009364117)
- [90] Malkusch S, Endesfelder U, Mondry J, et al. Coordinate-based colocalization analysis of single-molecule localization microscopy data. *Histochem Cell Biol*. 2012;137(1):1–10. doi: [10.1007/s00418-011-0880-5](https://doi.org/10.1007/s00418-011-0880-5)
- [91] Ovesny M, Křížek P, Borkovec J, et al. ThunderSTORM: a comprehensive ImageJ plug-in for PALM and STORM data analysis and super-resolution imaging. *Bioinformatics*. 2014;30(16):2389–2390. doi: [10.1093/bioinformatics/btu202](https://doi.org/10.1093/bioinformatics/btu202)
- [92] Cox J, Mann M. MaxQuant enables high peptide identification rates, individualized p.p.b.-range mass accuracies and proteome-wide protein quantification. *Nat Biotechnol*. 2008;26(12):1367–1372. doi: [10.1038/nbt.1511](https://doi.org/10.1038/nbt.1511)
- [93] Tyanova S, Temu T, Cox J. The MaxQuant computational platform for mass spectrometry-based shotgun proteomics. *Nat Protoc*. 2016;11(12):2301–2319. doi: [10.1038/nprot.2016.136](https://doi.org/10.1038/nprot.2016.136)
- [94] Cox J, Neuhauser N, Michalski A, et al. Andromeda: a peptide search engine integrated into the MaxQuant environment. *J Proteome Res*. 2011;10(4):1794–1805. doi: [10.1021/pr101065j](https://doi.org/10.1021/pr101065j)
- [95] Schwanhauser B, Busse D, Li N, et al. Global quantification of mammalian gene expression control. *Nature*. 2011;473(7347):337–342. doi: [10.1038/nature10098](https://doi.org/10.1038/nature10098)
- [96] Tyanova S, Temu T, Sinitcyn P, et al. The Perseus computational platform for comprehensive analysis of (prote)omics data. *Nat Methods*. 2016;13(9):731–740. doi: [10.1038/nmeth.3901](https://doi.org/10.1038/nmeth.3901)
- [97] Ginestet C. ggplot2: elegant graphics for data analysis. *J R Stat Soc Ser A Stat Soc J R STAT SOC A STAT*. 2011;174:245–245. doi: [10.1111/j.1467-985X.2010.00676_9.x](https://doi.org/10.1111/j.1467-985X.2010.00676_9.x)
- [98] Perez-Riverol Y, Bai J, Bandla C, et al. The PRIDE database resources in 2022: a hub for mass spectrometry-based proteomics evidences. *Nucleic Acids Res*. 2022;50(D1):D543–D552. doi: [10.1093/nar/gkab1038](https://doi.org/10.1093/nar/gkab1038)